

1 **Title: Formin-2 drives intracellular polymerisation of actin filaments enabling correct segregation**  
2 **of apicoplasts in *Plasmodium falciparum* and *Toxoplasma gondii*.**

3 Johannes Felix Stortz<sup>T1</sup>, Mirko Singer<sup>2</sup>, Jonathan M Wilkes<sup>1</sup>, Markus Meissner<sup>\*2</sup> and Sujaan Das<sup>T\*1,2</sup>

4 <sup>T</sup>These authors contributed equally

5 <sup>\*</sup>To whom correspondence should be addressed

6 [Sujaan.Das@glasgow.ac.uk](mailto:Sujaan.Das@glasgow.ac.uk)

7 [Markus.Meissner@para.vetmed.uni-muenchen.de](mailto:Markus.Meissner@para.vetmed.uni-muenchen.de)

8 **Affiliations**

9 <sup>1</sup>Wellcome Centre for Molecular Parasitology, Institute of Infection, Immunity & Inflammation,  
10 Glasgow Biomedical Research Centre, University of Glasgow, 120 University Place, Glasgow, G12  
11 8TA, UK. <sup>2</sup>Faculty of Veterinary Medicine, Ludwig-Maximilians-University Munich, Germany

12

13

14

15

16

17

18

19

20

21 **Abbreviations:**

22 C2, Compound 2; FV, food vacuole; F-actin, filamentous actin; PfACT1, *P. falciparum* actin-1; PfFRM1,  
23 *P. falciparum* Formin-1; PfFRM2, *P. falciparum* Formin-2; TgFRM1, *Toxoplasma gondii* Formin-1;  
24 TgFRM2, *Toxoplasma gondii* Formin-2; PV, parasitophorous vacuole; RAP, rapamycin; RON4, rhoptry  
25 neck protein-4; TJ, tight junction, IMC, inner membrane complex. PCR, Polymerase chain reaction;  
26 IFA, (indirect) Immunofluorescence assay; HA, Haemagglutinin; YFP, yellow fluorescent protein; RT,  
27 room temperature.

28 **Abstract**

29 Pathogenic obligate-intracellular apicomplexan parasites possess an essential chloroplast-like  
30 organelle called the apicoplast that undergoes division and segregation during replication. Parasite  
31 actin is essential during intracellular development, implicated in vesicular transport, parasite  
32 replication and apicoplast inheritance. However, the inability to visualise live actin dynamics in  
33 apicomplexan parasites limited functional characterisation of both filamentous-actin (F-actin) and  
34 actin regulatory factors. Apicomplexans possess at least two distinct formins, Formin-1 and Formin-  
35 2, predicted to serve as actin-nucleating factors, and previously implicated in regulating gliding  
36 motility and host cell invasion. Here, we expressed chromobodies and validated them as F-actin-  
37 binding sensors in *Plasmodium falciparum* and characterised the *in vivo* dynamics of the F-actin  
38 network. The F-actin network could be modulated chemically and disrupted by conditionally deleting  
39 the *actin-1* gene. In a comparative approach, we demonstrate that Formin-2 is closely associated  
40 with apicoplasts and with the F-actin network in *P. falciparum* and *Toxoplasma gondii*.  
41 Consequently, disruption of Formin-2 resulted not only in an apicoplast segregation defect, but also  
42 in complete abrogation of F-actin dynamics in intracellular parasites. Together, our results strongly  
43 indicate that Formin-2-mediated filament formation is the common primary mechanism for F-actin  
44 nucleation during apicomplexan intracellular growth effecting apicoplast segregation.

## 45 **Introduction**

46 The phylum Apicomplexa includes a variety of obligate intracellular parasites, which invade into and  
47 replicate inside mammalian cells, causing immense disease burden in humans and in commercially  
48 important livestock. One of its notorious members, the malaria parasite *Plasmodium falciparum*, is a  
49 major health concern in developing nations, causing ~500,000 deaths annually (White,  
50 Pukrittayakamee et al. 2014). Another member, *Toxoplasma* is a highly successful parasite infecting  
51 almost a third of the global human population and can be fatal in immunocompromised patients  
52 (Torgerson and Mastroiacovo 2013). There is limited success in the development of vaccines against  
53 these parasites and the current drugs are associated with drug resistance, making it crucial to  
54 investigate novel biological targets.

55 Actin is one of the most abundant proteins in eukaryotic cells. Due to its ability to form polymers,  
56 this cytoskeletal protein is involved in numerous processes such as cell motility, cytokinesis,  
57 organellar and vesicular transport, secretion and endocytosis (Svitkina 2018). Actins encoded by  
58 apicomplexan parasites are highly divergent compared to canonical actins from other eukaryotes  
59 (Douglas, Nandekar et al. 2018). *In vitro*, apicomplexan actins form only short, unstable polymers  
60 due to different polymerisation kinetics, caused by variation of certain key amino acids, otherwise  
61 conserved in metazoans (Kumpula and Kursula 2015). However, until recently an analysis of F-actin  
62 localisation and dynamics in apicomplexan parasites was hindered by the unavailability of F-actin  
63 sensors (Tardieux 2017), a limitation recently overcome by the expression of F-actin binding  
64 chromobodies in *T.gondii* (Periz, Whitelaw et al. 2017). Intriguingly, in this parasite, F-actin can form  
65 an extensive intra-vacuolar network that appears to be involved in material exchange and  
66 synchronisation of parasite division (Periz, Whitelaw et al. 2017).

67 Until recently, studies on apicomplexan F-actin focused on its critical role during host cell invasion  
68 and gliding motility (Soldati, Foth et al. 2004, Baum, Gilberger et al. 2008), where it is believed to  
69 provide the force for both processes (Frenal, Dubremetz et al. 2017). However, recent studies using

70 conditional mutants for *actin-1* in two apicomplexans, *P. falciparum* and *T. gondii* highlight  
71 additional critical roles of F-actin during intracellular parasite development (Das, Lemgruber et al.  
72 2017, Periz, Whitelaw et al. 2017, Whitelaw, Latorre-Barragan et al. 2017). Intriguingly, some  
73 functions, such as inheritance of the chloroplast-like organelle, the apicoplast, appears to be  
74 conserved (Andenmatten, Egarter et al. 2013, Egarter, Andenmatten et al. 2014, Das, Lemgruber et  
75 al. 2017, Whitelaw, Latorre-Barragan et al. 2017), while differences for the dependency of F-actin  
76 can be observed for other critical steps of the asexual life cycle. For example, host cell invasion is  
77 possible without *actin-1* (albeit at highly reduced levels) in case of *T. gondii* (Andenmatten, Egarter  
78 et al. 2013, Egarter, Andenmatten et al. 2014, Whitelaw, Latorre-Barragan et al. 2017), while it is  
79 completely blocked in case of *P. falciparum* (Das, Lemgruber et al. 2017). In contrast, *P. falciparum*  
80 does not require actin dynamics for egress from the host cell (Das, Lemgruber et al. 2017, Perrin,  
81 Collins et al. 2018), while it is essential for *T. gondii*.

82 Of the two actin genes present in *P. falciparum* (Gardner, Hall et al. 2002), only *actin-1* (*pfact1*) is  
83 expressed in all life-cycle stages and is the only actin expressed during asexual replicative stages,  
84 whereas *actin-2* expression is confined to the sexual gametocyte and insect stages (Vahokoski,  
85 Bhargav et al. 2014). *P. falciparum* undergoes a 48h asexual replicative cycle in the intermediate  
86 human host where it invades into, grows and replicates within erythrocytes, causing all clinical  
87 manifestations of the disease. After invasion, the merozoite form of the parasite (similar to *T. gondii*  
88 tachyzoites) establishes itself within a parasitophorous vacuole (PV), loses its ovoid shape to become  
89 amoeboid and feeds on host haemoglobin creating a food vacuole (FV) where haem is detoxified  
90 (Gruring, Heiber et al. 2011). The parasite then replicates by a process best described as internal  
91 budding, where daughter parasites develop within the mother (Francia and Striepen 2014). In the  
92 case of *T. gondii*, only two daughters are formed at a time in a process called endodyogeny. In  
93 contrast, malaria replication within the erythrocyte, termed schizogony, results in the formation of  
94 16-32 merozoites at once. Towards the end of a replicative cycle the parasite *de novo* forms its  
95 invasion-related organelles: the inner membrane complex (IMC), micronemes and rhoptries. In

96 contrast, parasite mitochondria and the apicoplast undergo growth and division and are trafficked  
97 into each daughter cell (Bannister, Hopkins et al. 2000). Although endodyogeny and schizogony  
98 appear very different, it is believed that both processes are very similar and use conserved molecular  
99 machinery. Indeed, independent studies identified the same factors to be critical for both replicative  
100 modes (Francia and Striepen, 2014).

101 Despite this, it could be assumed that differences, especially with respect to vesicular transport  
102 processes such as endocytosis and intravacuolar parasite communication, exist to adapt to different  
103 replication modes. This puts F-actin in the spotlight, since it plays a central role in these processes, as  
104 is the case in other eukaryotes (Svitkina 2018). We recently characterised a conditional mutant of  
105 PfACT1 and observed that in good agreement with the function of actin in *T. gondii* (Andenmatten,  
106 Egarter et al. 2013), inheritance of the apicoplast is compromised during schizogony (Das, Lemgruber  
107 et al. 2017). While the phenotypic analysis of conditional mutants is useful to identify conserved and  
108 unique functions of F-actin in apicomplexans, the inability to visualise F-actin in these parasites led  
109 to models, sometimes conflicting with each other and with the canonical behaviour of F-actin in  
110 other eukaryotes.

111 Common actin-labelling probes such as Phalloidin do not label apicomplexan actin and LifeAct could  
112 not be successfully expressed in these parasites (Periz, Whitelaw et al. 2017). Recently, actin-binding  
113 single-domain nanobodies tagged to fluorescent probes, called chromobodies were successfully  
114 expressed in *T. gondii* and shown to have minimal effect on actin dynamics (Periz, Whitelaw et al.  
115 2017), as also demonstrated in other eukaryotic cells (Rocchetti, Hawes et al. 2014, Panza, Maier et  
116 al. 2015, Melak, Plessner et al. 2017).

117 Here we adapted this technology to *P. falciparum* and demonstrate for the first time the localisation,  
118 dynamics and role of F-actin dynamics for parasite development in asexual stages. Interestingly, we  
119 find F-actin closely associated with the apicoplast throughout intracellular growth, leading to the  
120 question of which actin regulatory proteins are involved in this process. Most actin nucleation

121 proteins such as the Arp2/3 complex and the WAVE/WASP complex, and actin cross-linkers such as  
122  $\alpha$ -actinin and fimbrin are missing in apicomplexans (Baum, Papenfuss et al. 2006, Schuler and  
123 Matuschewski 2006). Two conserved nucleators found in *P. falciparum* are the formins, Formin-1  
124 (PfFRM1) and Formin-2 (PfFRM2) which localise to distinct compartments in the cell (Baum, Tonkin  
125 et al. 2008). Orthologs of both formins have been implicated in host cell invasion in *T.gondii* (Daher,  
126 Plattner et al. 2010), with *T. gondii* Formin-2 (TgFRM2) also being implicated in apicoplast  
127 maintenance (Jacot, Daher et al. 2013) – leading to inconsistencies in reports and questions whether  
128 the two formins have conserved or divergent functions in both parasites.

129 Here we reanalysed the role of Formin-2 in *P. falciparum* and *T. gondii* and, in contrast to previous  
130 reports, demonstrate that it localises adjacent to apicoplasts in both parasites. Conditional  
131 disruption of Formin-2 not only results in a complete abrogation of actin dynamics in *P. falciparum*  
132 and *T. gondii*, it also leads to loss of the apicoplast. Together our study highlights a highly conserved  
133 role of Formin-2 in the intracellular development of apicomplexan parasites. Importantly, apicoplast  
134 loss appears to be not the only critical phenotype caused by Formin-2 depletion, since in *P.*  
135 *falciparum* the loss of fitness due to the deletion of PfFRM2 cannot be complemented by addition of  
136 isopentenyl pyrophosphate (IPP), the only essential metabolite produced by apicoplasts (Yeh and  
137 DeRisi 2011), suggesting other critical roles of Formin2-mediated actin nucleation in these parasites.

138

## 139 **Results**

### 140 **1. Cellular expression of chromobodies in *P. falciparum* enables the visualisation of an actin** 141 **network throughout the asexual development of *P. falciparum* and in gametocytes.**

#### 142 **a. Chromobodies label F-actin structures in *P. falciparum* asexual stages and in gametocytes.**

143 Chromobodies were expressed under the *heat shock protein 86 (hsp86)* promoter (Crabb and  
144 Cowman 1996) to obtain expression throughout the 48h asexual life cycle. We succeeded in

145 generating parasites stably expressing chromobodies tagged either with the emerald tag (CB-EME)  
146 or the halo tag (CB-HALO), indicating that the expression of these constructs does not have a major  
147 deleterious impact on the fitness of *P. falciparum* (**Fig. 1A**), as previously reported for *Toxoplasma*  
148 (Periz, Whitelaw et al. 2017) and other eukaryotes . The halo tag allowed visualisation of F-actin in  
149 live parasites by use of the red ligand Halo-TMR. Dynamic filamentous structures were evident in  
150 both CB-EME and CB-HALO expressing parasites (**Fig 1B**) throughout the 48 hour life cycle (**Videos**  
151 **V1, V2, V3 and V4**). These structures could be completely disrupted by adding the F-actin  
152 destabilising drug cytochalasin-D (**Fig. 1B and Video V3**), demonstrating that chromobodies bind F-  
153 actin structures in *P. falciparum*. However, while both CB-versions labelled similar structures, we  
154 found that expression of CB-EME resulted in a better signal-to-noise ratio, probably because no  
155 permeable, fluorescent ligand needs to be added (**Fig.1B**). Therefore, for the rest of this study results  
156 for parasites expressing CB-EME are presented. Some F-actin structures were highly dynamic,  
157 changing within a time-scales of seconds, while other structures appeared stable over tens of  
158 seconds (**Video V3**). For better visualisation of F-actin structures, we used super-resolution  
159 microscopy (SR-SIM) which enabled us to observe a complex F-actin network in these parasites (**Figs.**  
160 **1C and S1**), similar to a network observed for *T.gondii* (Periz, Whitelaw et al. 2017). Since CB-EME  
161 was expressed from an episome, we quantified mean intensity of fluorescence in different cells and  
162 found it to be within a narrow range (**Fig. S1B**). Interestingly, F-actin was most prominent around the  
163 FV of the parasite (**Figs. 1C and S1**). When we co-stained the chromobody-labelled network with an  
164 antibody which specifically recognises parasite actin, we observed a rather cytosolic distribution  
165 with the antibody, although similar structures as seen with chromobody were apparent. This  
166 indicates that the antibody recognises monomeric globular actin (G-actin) along with F-actin, while  
167 the chromobody recognises primarily filamentous structures (**Fig. 1C and Fig S1**). In contrast to  
168 asexual parasites, gametocytes express both PfACT1 and actin-2, and exhibit F-actin staining along  
169 the length of the parasite and at the tips (Hliscs, Millet et al. 2015). Upon expression of CB-EME,  
170 gametocytes showed intense dynamic F-actin structures at their tips and running along the whole

171 body of the cell changing in seconds (**Fig. 1D and Video V5**). Importantly, this dynamic network  
172 appears very similar to the one reported by Hlisc et al., 2015, which has been shown to lie beneath  
173 the IMC of the gametocyte. It is important to note that chromobodies do not distinguish between  
174 PfACT1 and actin-2 and therefore the observed filaments could be built from both proteins.  
175 Together, our data show that expression of chromobodies does not cause significant phenotypic  
176 effects and allow reliable labelling of the F-actin cytoskeleton. We also confirm previous data  
177 obtained with antibodies directed against F-actin and show that during the gametocyte stage, F-  
178 actin forms a dynamic and extensive network that passes through the whole cell and is enriched at  
179 the tips of the parasite.

180 **b. Highly dynamic F-actin-rich filopodia-like structures extend outward from the periphery of**  
181 **growing parasites.**

182 After erythrocyte invasion, the parasite immediately loses its ovoid zoite structure and becomes an  
183 amoeboid ring-stage parasite. These young parasites are highly dynamic and can switch between  
184 various shapes forming multi-lobed structures, possibly mediated by their cytoskeletal networks  
185 (Gruring, Heiber et al. 2011). On observing chromobody-expressing parasites during ring and early  
186 trophozoite stages we noted F-actin rich projections at the periphery of ~60% parasites (n=50) (**Fig.**  
187 **2A, B and Video V2**). These F-actin projections are highly dynamic, changing in orders of seconds.  
188 Upon treatment with the F-actin depolymerising drug cytochalasin-D the peripheral dynamic F-actin  
189 protrusions disappeared (**Fig. 2A lower panel**), but the multilobed structures of the parasite were  
190 not disrupted (**Video V6**). The F-actin stabilising drug jasplakinolide also disrupted these filopodia-  
191 like extensions and resulted in formation of thick filaments (**Fig 4A lower panel**), implying the  
192 requirement of dynamic regulation of F-actin for maintenance of these projections. The physiological  
193 relevance of these filopodia is unclear at this point and further research into this phenomenon is  
194 required.

195 **c. Apical polymerisation of F-actin in merozoites following egress.**



196 Next, we wished to analyse the fate of the observed F-actin network upon parasite egress. We  
197 synchronised parasites with a 2-step Percoll and sorbitol treatment and harvested schizonts at 44h  
198 post-invasion. Reversible inhibitors of protein kinase G, Compound-1 and -2, stall schizont  
199 development at very mature stages without allowing them to undergo egress (Collins, Hackett et al.  
200 2013). We treated highly mature schizonts with Compound-2 to allow them to fully mature without  
201 undergoing egress for 4h. Upon washing away Compound-2, the parasites egressed normally with  
202 the concomitant appearance of F-actin accumulation at the apical tip of the parasite (**Fig. 2C, Video**  
203 **V4**). Cytochalasin-D treatment allowed normal egress of parasites, as previously observed (Video S8  
204 of (Weiss, Gilson et al. 2015)), but completely abrogated F-actin polymerisation at the apical tip (**Fig.**  
205 **2C**). Finally, we performed IFA on invading merozoites using rhoptry neck protein 4 (RON4) as  
206 junctional marker. We verified that F-actin accumulates just behind the RON4 ring (**Fig. 2D**)  
207 confirming previous observations (Riglar, Richard et al. 2011, Angrisano, Riglar et al. 2012).

#### 208 **d. Chromobody labelled F-actin structures disappear upon disruption of PfACT1.**

209 Although *P. falciparum* parasites possess two actin genes *pfact1* and *pfact2*, PfACT1 is the only  
210 protein expressed during the asexual life cycle (Vahokoski, Bhargav et al. 2014). In order to confirm  
211 that chromobodies label authentic F-actin structures based on polymerisation of PfACT1, we  
212 transfected the chromobody constructs CB-EME (**Fig. 3A**) and CB-HALO (**Fig. S2B, C**) into a  
213 conditional mutant of PfACT1 (loxPACT1) (Das, Lemgruber et al. 2017) (**Fig 3A**). Upon activation of  
214 DiCre with rapamycin, the *pfact1* locus is excised together with loss of PfACT1 protein within 35h  
215 (Das, Lemgruber et al. 2017). Upon disruption of *pfact1* in 1h-old ring stages, CB-EME (**Fig. 3B, D, E,**  
216 **Video V7**) and CB-HALO (**Fig. S2**) labelled F-actin structures completely disappeared in late  
217 trophozoites and schizonts and closely resembled parasites treated with cytochalasin-D (**Fig. 1B**). As  
218 previously reported (Das, Lemgruber et al. 2017), PfACT1-disrupted parasites could not invade new  
219 erythrocytes (**Fig. 3C**).

220 We previously found that apicoplast inheritance depends on PFACT1 (Das, Lemgruber et al. 2017). In  
221 order to determine the localisation of F-actin during apicoplast segregation we used deconvolution  
222 microscopy on fixed parasites stained with the apicoplast marker CPN60, which revealed a close  
223 apposition of apicoplasts with F-actin structures (**Fig 3F DMSO**). Upon disruption of PFACT1, a defect  
224 in apicoplast segregation was apparent (**Fig 3F RAP**) recapitulating the phenotype observed  
225 previously (Das, Lemgruber et al. 2017). Super-resolution microscopy confirmed that actin filaments  
226 labelled by CB-EME are closely placed next to migrating apicoplasts (**Fig S1, lower panel**). In contrast,  
227 no obvious defects in mitochondria segregation could be detected in PFACT1-disrupted parasites  
228 (**Fig. 3E and Video V7**) as previously reported (Das, Lemgruber et al. 2017), implying that unlike  
229 apicoplasts, mitochondria do not require F-actin for migration into daughter cells. IMC markers  
230 GAP45 and MTIP showed normal staining in CB-EME expressing parasites (**Fig S1**).

231 We reasoned that since most canonical actin filament stabilising and nucleating proteins are absent  
232 in Apicomplexa, the parasite must depend on formins for F-actin assembly. Previously, PFFRM1 has  
233 been localised to the invasion junction and PFFRM2 to the cytosol (Baum, Tonkin et al. 2008). Since  
234 we observed the intracellular F-actin network in the cytosol, we speculated that Formin-2 is the  
235 main nucleator of F-actin during intracellular parasite development, even though it has been  
236 implicated in host cell invasion in the case of *T.gondii* (Daher, Plattner et al. 2010).

## 237 **2. Apicomplexan Formin-2 sequences contain a PTEN-C2-like domain found usually in plant** 238 **formins**

239 Formins possess a formin homology (FH) 1 and an FH2 domain, which nucleate actin monomers as  
240 well as elongate unbranched F-actin by continuous processive binding to the barbed end of the  
241 filament (Courtemanche 2018). In a previous report (Baum, Tonkin et al. 2008), only FH1/FH2  
242 domains were described for apicomplexan formins. Here, we queried for presence of known PFAM  
243 domains using NCBI conserved domain search and in addition to FH1/FH2, found tetratricopeptide  
244 repeat (TPR) domains in both PFFRM1 and TgFRM1, while a PTEN C2-like domain was recognised in

245 PFFRM2 and TgFRM2 (**Fig. 4A**). This led us to hypothesise that Formin-1 and Formin-2 with different  
246 N-terminal domains diverged early in evolution and different domain organisations have been  
247 retained for different functions. We queried for various FH2-domain containing proteins from  
248 Apicomplexans and found that Formin-2-like sequences are found in a different clade from Formin-  
249 1-like sequences (**Fig. 4B**), as also previously noted (Baum, Tonkin et al. 2008). Strikingly, the PTEN-  
250 C2-domain (or a diverged PTEN-C2 domain) was found only in Formin-2-like sequences (**Fig. 4B**).  
251 Interestingly, PTEN-C2 domains are important for membrane recruitment (Das, Dixon et al. 2003)  
252 and it has been shown to be recruited to rice chloroplast membranes (Zhang, Zhang et al. 2011),  
253 leading us to hypothesise that a similar mechanism operates for apicoplast recruitment of Formin-2  
254 sequences in apicomplexans.

## 255 **2. *Plasmodium* and *Toxoplasma* Formin-2 localise adjacent to apicoplasts**

256 In order to characterise the role of Formin-2 in detail, we decided to perform a comparative analysis  
257 in both *T.gondii* and *P. falciparum*. Therefore, we epitope tagged Formin-2 in both parasites. For  
258 tagging in *T.gondii* we used a CRISPR/Cas9-based strategy to introduce a 3x hemagglutinin (3HA) tag  
259 at the TgFRM2 C-terminus (**Fig. 4C**) and confirmed correct integration by diagnostic PCR (**Fig 4D**).  
260 Upon colocalisation with the anti-apicoplast antibody G2-Trx (Biddau and Sheiner, unpublished), we  
261 found TgFRM2 to be localised adjacent to apicoplasts (**Fig, 4E**), which was confirmed by super-  
262 resolution microscopy (**Fig. 4F**). For localisation of PFFRM2, we simultaneously epitope tagged and  
263 floxed PFFRM2 by single cross-over homologous recombination in a DiCre-expressing parasite strain  
264 (**Fig. 4G**) and confirmed integrants by diagnostic PCR (**Fig. 4H**). Integrants were cloned by limiting  
265 dilution and two distinct clones of 'LoxPpfformin2' were used for phenotypic characterisation.  
266 PFFRM2 showed a punctate pattern in context of PfACT1 antibody staining (**Fig 4I**). Next, we checked  
267 for PFFRM2 localisation in relation to the apicoplast and observed a close apposition of the  
268 apicoplasts with the PFFRM2 staining throughout the 48h malaria life-cycle (**Fig. 4J**), which was

269 confirmed by super-resolution microscopy (**Fig. 4K**). In conclusion, both *Toxoplasma* and *P.*  
270 *falciparum* Formin-2 localises adjacent to apicoplasts.

271 **3. DiCre-mediated conditional disruption of Formin-2 causes a defect in apicoplast segregation in**  
272 ***P. falciparum***

273 Next, we wished to evaluate the fate of *P. falciparum* upon conditional DiCre-mediated disruption of  
274 the *pffrm2* gene (**Fig 5A**). 1h old tightly synchronised ring stage parasites were divided into two  
275 flasks and either pulse-treated with rapamycin (RAP) or DMSO (control) for 4h and their phenotype  
276 determined at 44h post RAP-treatment. Excision was determined by diagnostic PCR of the genomic  
277 locus (**Fig 5B**) and fitness of the PffRM2 conditional knock out (KO) was measured by a growth curve  
278 which showed significant loss of viability (**Fig. 5C**). Loss of protein was ~90% as determined by  
279 Western blot (**Fig. 5D**) and was confirmed by IFA (**Fig. 5E**), which indicated a loss of protein in ~95%  
280 parasites (N=350). Giemsa stained PffRM2 KO parasites were dysmorphic with apparent inclusions  
281 of haemoglobin (**Fig. 5F, red arrows**). In order to determine the morphological defects in FRM2 KO  
282 parasites, we co-stained PffRM2 KO parasites with several organellar markers and were unable to  
283 see significant differences (not shown), except for apicoplast segregation (**Fig. 5G**). The number of  
284 parasites with normally segregated apicoplasts was significantly reduced, with a high percentage of  
285 cells showing collapsed or morphologically aberrant apicoplasts (**Fig 5G, H**). A range of apicoplast  
286 phenotypes was evident, from totally collapsed, intermediate to apparently normal (**Fig S3A**). To  
287 determine if the loss of viability of the PffRM2 KO parasites was solely due to loss of the apicoplast,  
288 we attempted to rescue the phenotype with 200µM isopentenyl pyrophosphate (IPP) which has  
289 been previously shown to complement growth in parasites lacking apicoplasts (Yeh and DeRisi 2011).  
290 However, we did not see any improvement in viability, indicating that the loss of fitness is due to  
291 additional defects caused by abrogation of F-actin dynamics in the parasite. We determined number  
292 of nuclei in 44h PffRM2 KO parasites and found a significant decrease in the number of nuclei (**Fig.**  
293 **S3B**), indicating a developmental defect. Since PfACT1 is required for normal cytokinesis (Das,

294 Lemgruber et al. 2017), we interrogated if the IMC is normally formed in PFRM2 KO parasites. We  
295 purified mature schizonts on a 70% Percoll cushion and determined by IFA that IMC formation was  
296 compromised in these parasites, with normal IMC staining dropping from  $58\pm 8\%$  in WT to  $19\pm 8\%$  in  
297 PFRM2 KOs (**Fig. S3C, D**). When we allowed PFRM2 KO parasites to egress and compared them to  
298 control parasites, we found conjoined merozoites in PFRM2 KOs, a defect previously seen in PFACT1  
299 KO parasites (Das, Lemgruber et al. 2017), indicating that PFRM2 and PFACT1 coordinate cytokinesis  
300 in *P. falciparum*.

301

#### 302 **4. DiCre-mediated disruption of Formin-2 abrogates the actin network in *P. falciparum*** 303 **trophozoites**

304 Next, we wished to determine whether F-actin assembly and dynamics is interfered upon deletion of  
305 PFRM2 and if this directly affects apicoplast segregation. We expressed CB-EME in LoxPpfformin2 to  
306 generate the line LoxPpfformin2/CBEME (**Fig. 6A**) and visualised actin filaments (**Fig 6B, DMSO**). As  
307 observed in wild-type parasites (**Fig 1**), F-actin was decorated with punctate PFRM2-HA staining (**Fig**  
308 **S4, Pf**). Upon DiCre-mediated excision in ring stages, we saw a complete abrogation of the dynamic  
309 F-actin network in mature schizont stage parasites (**Fig 6B RAP**), which dropped from exhibiting an F-  
310 actin network in  $92\pm 5\%$  cells in WT to  $5\pm 4\%$  cells in PFRM2 KO (**Fig. 6C**). Furthermore, we confirmed  
311 the apicoplast phenotype in parasites expressing CB-EME (**Fig 6D**).

312 Interestingly, we observed that actin-rich filopodia formed at the cell-periphery (see also **Fig. 2A, B**)  
313 disappeared upon PFRM2 disruption (**Fig. 6E**), providing a mechanism for this novel phenomenon.

314 Since PFRM1 was localised to the parasite apex/ invasion junction during host cell entry (Baum,  
315 Tonkin et al. 2008), we reasoned that apical polymerisation of F-actin should not be affected in  
316 PFRM2 KO parasites, if indeed the two formins perform distinct functions in their distinct  
317 localisations. To this end, we allowed mature schizonts to egress and release free merozoites and

318 subsequently imaged them by live fluorescence microscopy. Consistent with this hypothesis, we  
319 found that the ability of F-actin polymerisation at the parasite apex was not compromised in PfFRM2  
320 KO parasites (**Fig. 6F**), strongly indicating distinct functions of PfFRM1 and PfFRM2.

321

## 322 **5. Conditional deletion of Formin-2 in *Toxoplasma* disrupts apicoplast segregation and F-actin** 323 **dynamics**

324 Finally, in order to assess if the function of Formin-2 is conserved in apicomplexan parasites, we  
325 analysed its role in *T.gondii*. We first checked the localisation of TgFRM2 with respect to the F-actin  
326 network. Similar to *P. falciparum*, TgFRM2-HA formed puncta on CB-EME labelled F-actin network  
327 within the parasite, where it appeared to co-localise with a polymerisation centre (**Fig. S4 Tg**). Next,  
328 we simultaneously floxed *tgfrm2* together with addition of C-terminal YFP tag to create the  
329 LoxPTgFRM2 line (**Fig. 7A**). This enabled us to confirm localisation of Formin-2 and determine the  
330 comparative effect of a conditional KO in *Toxoplasma*. Integration of the C-terminal YFP-tag and  
331 *LoxP* sites was confirmed by diagnostic PCR, as was excision of the *tgfrm2* locus upon RAP-treatment  
332 (**Fig S5A**). For the localisation of TgFRM2 it was necessary to stain fixed parasites with a YFP-  
333 antibody, suggesting low expression levels of TgFRM2. We confirmed localisation of TgFRM2  
334 adjacent to the apicoplast (**Fig 7B upper panel**). Upon RAP-treatment, excision of TgFRM2 was  
335 apparent in 14% (clone A) or 33% (clone B) of parasites, as assessed by quantification of parasites  
336 where no TgFRM2 could be detected by IFA. Importantly, loss of TgFRM2 staining correlated with an  
337 apicoplast segregation phenotype in the majority of parasites (**Fig 7B lower panel, 42.4 % [n=66] in**  
338 **clone A and 70% [n=100] in clone B**). A baseline apicoplast segregation phenotype was observed in  
339 2% (clone A) or 1% (clone B) of vacuoles in the control population. Transient expression of CB-EME in  
340 LoxPTgFRM2 parasites enabled us to image F-actin and demonstrated that, in good agreement with  
341 data from *P. falciparum*, intracellular F-actin was adjacent to the apicoplast (**Fig 7C control**).  
342 Intriguingly, excision of TgFRM2 (**Fig. 7C RAP**) led to the disappearance of intracellular F-actin, while

343 (in contrast to *P. falciparum*), the intravacuolar F-actin network was still present (**Fig.7C**), indicating  
344 that another formin, potentially Formin-3 (Daher, Klages et al. 2012), which is not present in  
345 *P.falciparum*, contributes to its formation.

346

## 347 **Discussion**

348 Due to the unconventional behaviour of apicomplexan actin, the visualisation of actin filaments in *P.*  
349 *falciparum* was hampered by the lack of reagents and F-actin sensors that do not interfere  
350 significantly with F-actin polymerisation and depolymerisation. Therefore, previous attempts to use  
351 established indicators such as Life-Act from other eukaryotic systems failed (Tardieux 2017). In a  
352 recent study it was shown that actin-binding nanobodies fused to epitope tags could be expressed in  
353 *Toxoplasma gondii*, allowing for the first time to analyse F-actin localisation and dynamics in living  
354 parasites (Periz, Whitelaw et al. 2017). Here we successfully adapted this technology to *P. falciparum*  
355 using two different epitope tags, the halo tag and the emerald tag. This allowed us to visualise F-  
356 actin throughout the asexual life-cycle of *P. falciparum* and in gametocytes without causing any  
357 aberrant phenotypes, suggesting that this reagent, as in the case of *T.gondii* (Periz, Whitelaw et al.  
358 2017) and all other eukaryotes tested so far (Melak, Plessner et al. 2017) does not significantly  
359 interfere with F-actin dynamics. Importantly, validation of this reagent using either F-actin  
360 modulating drugs or a conditional mutant for PfACT1 led to expected results and phenotypes,  
361 demonstrating that F-actin dynamics is finely balanced in the parasite. Since expression of  
362 chromobodies does not interfere with parasite viability, it can be assumed that its influence on F-  
363 actin dynamics is at best minor, potentially leading to slightly altered F-actin dynamics. Similar  
364 influences of F-actin sensors have been observed and discussed in other eukaryotes (Melak, Plessner  
365 et al. 2017). As a general rule, any F-actin sensor will influence F-actin dynamics or might not be able  
366 to stain all F-actin structures. In this respect, F-actin binding nanobodies are a novel tool and appear  
367 to have only minimal effects on F-actin dynamics compared to other sensors (Melak, Plessner et al.

2017), which might explain that they are well tolerated in Apicomplexans, where rapid F-actin dynamics appears to be critical for parasite viability. Using this novel tool, we not only demonstrate here that F-actin can be found in very close proximity of apicoplasts, we also demonstrate a novel function of F-actin during the intracellular development of *P. falciparum*: formation of highly dynamic, filopodia-like structures. While the role of this process is currently unknown, we show that interference with F-actin dynamics, either by addition of actin-modulating drugs or conditional mutants for PfACT1 or PffRM2, led to a complete blockade in the formation of these structures.

Super-resolution imaging revealed a complex F-actin network in *P. falciparum*, similar to that observed in *T.gondii* (Periz, Whitelaw et al. 2017) with extensive filaments around the FV. Importantly, our previous characterisation of a conditional mutant for PfACT1 highlighted the diverse functions of actin during the asexual life cycle of the parasite (Das, Lemgruber et al. 2017), which perfectly correlates to the localisation and dynamics found here using chromobody-expressing parasites. PfACT1 is essential for *P. falciparum* invasion into erythrocytes and we show for the first time the temporal and spatial dynamics of actin polymerisation by live microscopy prior to invasion. Despite a growing body of evidence suggesting the importance of calcium signalling and phosphorylation of IMC proteins by kinases such as CDPK1 and PKA (Baker, Drought et al. 2017, Kumar, Kumar et al. 2017) during invasion, what triggers the polymerisation of actin is largely unknown. Our data suggest that early signalling events just after egress are a trigger for actin-polymerisation at the apical end. This is likely to be mediated by an apically resident nucleator of F-actin, a likely candidate being Formin-1, since PffRM2 KO parasites could still polymerise actin at the apical end, as demonstrated in this study.

Therefore, the expression of chromobodies in *P. falciparum* allows us to phenotypically probe the state of the F-actin network *in vivo* in a rapid and robust manner. F-actin can be clearly visualised during growth, in invading merozoites and in gametocytes – opening up many avenues for further research. Using this novel tool, combined with powerful reverse genetics made possible by the DiCre



393 system (Collins, Das et al. 2013) we show here that Formin-2 in both *Toxoplasma* and *Plasmodium* is  
394 required for the intracellular polymerisation of F-actin, a mechanism employed by the parasite for  
395 correct segregation of apicoplasts. Using extensive bioinformatic searches within alveolates, we  
396 found the presence of a PTEN-C2-like domain only in apicomplexan Formin-2 sequences. This  
397 domain has been demonstrated in rice to be responsible for Formin-2 targeting to chloroplast  
398 membranes (Zhang, Zhang et al. 2011). It is therefore likely that the apicomplexan PTEN-C2-like  
399 domain is used for apicoplast recruitment of apicomplexan Formin-2.

400 Interestingly, while we found that the role of Formin-2 appears to be conserved in *T.gondii* and *P.*  
401 *falciparum* for intracellular F-actin dynamics and apicoplast inheritance (**Fig. 8**), in the case of *T.*  
402 *gondii* the intravacuolar F-actin network is still formed, suggesting that *T.gondii* and potentially other  
403 coccidia have additional, compensatory mechanisms at their disposal to form this network, which  
404 appears to be critical for material exchange, synchronised replication of parasites and host cell  
405 egress (Periz, Whitelaw et al. 2017).

406 In conclusion, we show here that chromobodies can be used to determine F-actin dynamics in  
407 apicomplexan parasites and will form the basis for functional *in vivo* studies of other actin regulatory  
408 proteins found in apicomplexans. Furthermore, they can be used as an efficient tool to probe for  
409 drugs specifically interfering with F-actin dynamics in apicomplexans.

410

## 411 **Experimental procedures**

### 412 **1. Culture and transfection of *P. falciparum***

413 *P. falciparum* was cultured in RPMI 1640 with Albumax (Invitrogen) and schizonts were purified on a  
414 bed of 70% Percoll as described previously (Blackman 1994). About 10 µg of plasmid was ethanol  
415 precipitated and resuspended in 10 µL sterile buffer TE (Qiagen). The Amaxa™ P3 primary cell 4D  
416 Nucleofector™ X Kit L (Lonza) was used for transfections. The input DNA was added to 100 µL P3

417 primary cell solution, mixed with 10-20  $\mu$ L of packed synchronous mature schizonts and added to the  
418 cuvette, which was electroporated in a 4D-Nucleofector machine (Lonza) using the program FP158.  
419 The transfected schizonts were rapidly added to 2 mL of complete medium (RPMI with Albumax  
420 supplemented with glutamine) containing erythrocytes at a haematocrit of 15%, and left shaking in a  
421 shaking incubator at 37°C for 30 min. Finally the cultures were supplemented with 7 mL of complete  
422 RPMI medium to obtain a final haematocrit of 3% and incubated overnight at 37°C in a small angle-  
423 necked flask (Nunc™). Parasites were selected by use of appropriate drug medium. The culture  
424 medium was subsequently exchanged every day for the next 4 days to remove cell debris which  
425 accumulates during electroporation and then twice a week until parasites were detected by Giemsa  
426 smear. Drug-resistant parasites were generally detectable in thin blood films 2-3 weeks post-  
427 transfection. After this, parasite stocks (at ~5% ring parasitaemia) were cryopreserved in liquid  
428 nitrogen. Lines were then cloned by limiting dilution using a simple plaque assay (Thomas, Collins et  
429 al. 2016).

## 430 **2. Cloning and expression of chromobodies in *P. falciparum***

431 The CB-HALO and CB-EME plasmid consists of a sequence encoding actin chromobody from  
432 Chromotek followed downstream by an in frame sequence encoding Halo (Promega) or the emerald  
433 tag. CB-EME and CB-HALO sequences were amplified by PCR and cloned into the vector pB-  
434 map2gfpdd (Nicholas Brancucci, unpublished) via restriction sites NheI and HindIII to remove the  
435 map2gfpdd sequence and put the CB-sequences under the *hsp86* promoter. The resulting plasmids  
436 pB-CBEME and pB-CBHALO were sequenced on both strands to confirm correct nucleotide  
437 sequences. These constructs were transfected as described into the loxPACT1 parasite clone B2 (Das,  
438 Lemgruber et al. 2017) to obtain parasite lines LoxPPfACT1/CBEME, LoxPPfACT1/CBHALO and into  
439 the parental 1G5DiCre clone (Collins, Das et al. 2013) to obtain the line CBEME/1G5DiCre and  
440 CBHALO/1G5DiCre. Lines were selected with 2.5  $\mu$ g/mL blasticidin. CB-EME expression was visible by  
441 fluorophore excitation/emission in the green range and the HALO ligand was made visible by use of

442 the ligand HALO-TMR at 1:40,000 with excitation/emission in the red range. Alternatively antibodies  
443 were used against the HALO tag to stain for CB-HALO.

### 444 **3. *P. falciparum* IFA**

445 Thin blood films were made on glass slides and fixed in 4% paraformaldehyde in PBS for 20 min. The  
446 slides were then permeabilised with 0.1% Triton-X/PBS for 10 min, washed and blocked overnight in  
447 4% BSA/PBS. Antigens were labelled with suitable primary and secondary antibodies in 4% BSA/PBS  
448 with 5 min PBS washes in between. Slides were finally air dried and mounted with DAPI-Fluormount-  
449 G® (SouthernBiotech).

450 Staining of the RON4 junction in CB-EME expressing was performed by fixation and immunostaining  
451 in solution as described previously (Riglar, Richard et al. 2011).

452 For image acquisition, z-stacks were collected using a UPLSAPO 100× oil (1.40NA) objective on a  
453 Deltavision Core microscope (Image Solutions – Applied Precision, GE) attached to a CoolSNAP HQ2  
454 CCD camera. Deconvolution was performed using SoftWoRx Suite 2.0 (Applied Precision, GE).

455 An Elyra S1 microscope with Superresolution Structured Illumination (SR-SIM) (Zeiss) was used for  
456 super-resolution imaging.

### 457 **4. Time lapse microscopy of live *P. falciparum***

458 Video microscopy of *P. falciparum* schizont egress was performed as described previously (Collins,  
459 Hackett et al. 2013). Synchronised schizonts were Percoll® purified and treated with 1 µM C2 in  
460 RPMI medium with Albumax® (Gibco) for 4h. Microscopy chambers (internal volume ~80 µl) for  
461 observing live schizonts were built by adhering 22×64 mm borosilicate glass coverslips to microscope  
462 slides with strips of double-sided tape, leaving ~4 mm gaps at each end. C1 was washed off before  
463 video microscopy and the schizonts were immediately resuspended into warm (37°C) RPMI (with  
464 Albumax) and introduced by capillary action into the pre-warmed chamber. The chamber was

465 transferred to a temperature-controlled microscope stage at 37°C on a Deltavision Core microscope  
466 (Image Solutions – Applied Precision, GE). Images were routinely collected at 5 s intervals, beginning  
467 6 min 30 sec after washing off C1, over a total of 30 min.

468 Other than during egress, CB-EME and CB-HALO expressing parasites were imaged at intervals of 1  
469 sec.

## 470 **5. Bioinformatics**

471 Proteomes of interest (Table T2) were downloaded from the UniProt-KB website ([www.uniprot.org](http://www.uniprot.org)).  
472 These were concatenated into a single proteome sequence dataset. All sequence identifiers and  
473 annotations referred to are from UniProt Hidden Markov Models (PFAM profiles) PF02181.23  
474 (FH2.hmm, Formin Homology 2 Domain) and PF10409.9 (PTEN\_C2.hmm, C2 domain of PTEN  
475 tumour-suppressor protein) were downloaded from Pfam (El-Gebali, Mistry et al. 2018). These  
476 profiles were used with the HMMER package (HMMER 3.1b1 (May 2013); <http://hmmer.org/>) to  
477 search the proteome sequences (hmmsearch), and to align sequences of interest (hmmalign). The  
478 proteome sequence dataset was searched for FH2 domains (FH2.hmm) with hmmsearch, and  
479 sequences with regions scoring >28bits recorded. These sequences were retrieved from the dataset,  
480 and subjected to alignment against the FH2.hmm. The profile conformant subsequences were  
481 extracted from the alignment and this sequence set subjected to alignment using:  
482 1) hmmalign to FH2.hmm, 2) clustalw (Thompson, Higgins et al. 1994) 3) muscle (Edgar 2004) and 4)  
483 T\_Coffee. These multiple sequence alignments were combined and evaluated in T\_coffee (Keller,  
484 Kollmar et al. 2011) using the -aln and -special\_mode evaluate options of T\_coffee and the  
485 alignment edited to remove columns of average quality <4 and occupancy <30% (T\_coffee -  
486 other\_pg seq\_reformat option). Rooted neighbour-joining trees of Formin Homology type 2 domains  
487 (FH2) was constructed from this alignment (or subsets of it) using the SplitsTree program [version  
488 1.14.8,\*]. The proteome dataset was searched for the presence of PTEN\_C2 conformant sequences.  
489 As only an inconsistent subset of sequences were found in both PTEN\_C2 and FH2 selected

490 sequences; one such subsequence (A0A1A7VGT3\_PLAKH, residues 1096-1238) was used as the  
491 query of an iterative psi-blast [1], (E-value cutoff =10) using the proteome data set as the database.  
492 The program converged after 3 iterations. The sequences flagged by psi-blast as having PTEN\_C2-like  
493 sequence were compared with the sequences flagged by hmmsearch as having FH2 domains, and  
494 such sequences annotated on the phylogenetic tree.

## 495 **6. Creation of LoxPPfFRM2-HA and LoxPPfFRM2/CBEME strains**

496 To obtain conditional truncation of the *pffrm2* gene we used silent *loxP* sites within a heterologous  
497 *P. falciparum* intron loxPint (Jones, Das et al. 2016). We ordered from Geneart® a ~800 bp targeting  
498 sequence followed by the LoxPint module in the context AATTGTAG-LoxPint-ATAGCTTT followed by  
499 a recodonised version of rest of the 3' region of the gene together with a C-terminal 3HA tag. This  
500 ordered synthetic fragment was cloned into the pHH1-loxPMSP1 plasmid (Das, Hertrich et al. 2015)  
501 via restriction sites AflII and ClaI, replacing the *msp1* sequence with *pffrm2*, giving rise to the plasmid  
502 pHH1-LoxPintFormin2 (**Fig. 4G**). This was transfected into the DiCre expressing strain B11 (Perrin,  
503 Collins et al. 2018) and integrants selected by cycling on and off the drug WR99210 (Jacobus  
504 Pharmaceuticals, New Jersey, USA). The integrant line LoxPPfFRM2 was cloned by limiting dilution  
505 and two clones used for phenotypic characterisation. The strain LoxPPfFRM2/CBEME was created by  
506 transfecting the pB-CBEME plasmid into a LoxPPfFRM2-HA clone line and transfectants selected  
507 using the drug blasticidin (Sigma).

## 508 **7. Conditional truncation of *pfact1* and *pffrm2***

509 Various floxed parasite strains were synchronised by Percoll and sorbitol as previously described  
510 (Collins, Hackett et al. 2013). Briefly, schizonts were purified on a bed of 66% Percoll and allowed to  
511 reinvade into fresh erythrocytes for 1-2h. The remainder of the schizonts were removed by Percoll  
512 and the freshly invaded rings were subjected to 5% sorbitol for 7 min at 37°C to lyse any remaining  
513 schizonts. The tightly synchronised rings were divided into two flasks and pulse-treated for 4h at

514 37°C with 100 nM rapamycin or with 1% DMSO as control. The rings were then washed and returned  
515 to culture. Phenotypic analysis was performed primarily 44h post RAP-treatment unless stated  
516 otherwise.

517

## 518 **8. Culturing of *Toxoplasma* parasites and host cells**

519 Human foreskin fibroblasts (HFFs) (RRID: CVCL\_3285, ATCC) were grown on tissue culture-treated  
520 plastics and maintained in Dulbecco's modified Eagle's medium (DMEM) supplemented with 10%  
521 foetal bovine serum, 2 mM L-glutamine and 25 mg/mL gentamycin. Parasites were cultured on HFFs  
522 and maintained at 37° C and 5% CO<sub>2</sub>. Cultured cells and parasites were regularly screened against  
523 mycoplasma contamination using the LookOut Mycoplasma detection kit (Sigma) and cured with  
524 Mycoplasma Removal Agent (Bio-Rad) if necessary.

## 525 **9. Microscopy for *Toxoplasma***

526 Widefield images were acquired in z-stacks of 2 µm increments and were collected using an Olympus  
527 UPLSAPO 100× oil (1.40NA) objective on a Delta Vision Core microscope (AppliedPrecision, GE)  
528 attached to a CoolSNAP HQ2 CCD camera. Deconvolution was performed using SoftWoRx Suite 2.0  
529 (AppliedPrecision, GE). Further image processing was performed using ImageJ software.

530 Super-resolution microscopy (SR-SIM) was carried out using an ELYRA PS.1 microscope (Zeiss) as  
531 described previously (Periz et al., 2017). Images were acquired using a Plan Apochromat 63×, 1.4 NA  
532 oil immersion lens, recorded with a CoolSNAP HQ camera (Photometrics), and analysed using ZEN  
533 Black software (Zeiss) and ImageJ software.

## 534 **10. *Toxoplasma* IFA**

535 For immunofluorescence analysis, HFF monolayers infected with *Toxoplasma* parasites were grown  
536 on coverslips and fixed at the indicated time points in 4% paraformaldehyde for 20 min at RT.

537 Afterwards coverslips were permeabilised in 0.2% Triton X–100 in 1× PBS for 20 min, followed by  
538 blocking (3% BSA & 0.2% Triton X–100 in 1x PBS) for at least 30 min. The staining was performed  
539 using indicated combinations of primary antibodies for 1 h and followed by secondary Alexa Fluor  
540 488 or Alexa Fluor 594 conjugated antibodies (1:3000, Invitrogen–Molecular Probes) for another 45  
541 min, respectively. The primary antibodies used in this studies are anti-G2Trx (1:500, rabbit,  
542 apicoplast, Dr Lilach Sheiner), anti-HSP60/CPN60 (1:2000, rabbit, apicoplast, Dr Lilach Sheiner), anti-  
543 Atrx1 (1:500, mouse, apicoplast, Prof Peter Bradley), anti-HA (1:500, rat, Roche [cat# 1187431001])  
544 and anti-YFP (1:500, rabbit, Abcam [ab6556

#### 545 **11. Generation of the TgFRM2-HA and loxPTgFRM2-YFP strains in RH $\Delta$ ku80DiCre parasites**

546 Guide RNAs targeting the upstream region of TgFRM2 and the C-terminal region were designed  
547 using EuPaGDT (Ref: Duo Peng and Rick Tarleton. EuPaGDT: a web tool tailored to design CRISPR  
548 guide RNAs for eukaryotic pathogens. Microbial Genomics. 2015. doi: 10.1099/mgen.0.000033).  
549 These were cloned into a vector expressing a Cas9-YFP fusion as well as the specific gRNAs as  
550 previously described (Curt-Varesano, Braun et al. 2016). The designed gRNAs  
551 ACTTTTCATAGTATAGGAGG CGG and AATAGGGGTCTGTAGGTAA GGG bind 989 bp upstream of the  
552 start codon and 12 bp upstream of the stop codon of TgFRM2 respectively. To introduce the  
553 upstream LoxP site, the LoxP sequence ATAACCTCGTATAGCATACATTATACGAAGTTAT flanked with  
554 respective 33 bp homology on each side was ordered as a 100 bp primer (ThermoFischer Scientific).  
555 The repair template for the C-terminal tag (HA or YFP) was generated by PCR using Q5 polymerase  
556 (New England Biolabs) from template plasmids with 50 bp of target-specific homology introduced via  
557 the primer. All tags are flanked by the same sequence, the upstream linker sequence  
558 GCTAAAATTGGAAGTGGAGGA encoding for the amino acid sequence AKIGSGG, the tag itself, a stop  
559 codon and the LoxP sequence. The YFP tag is superfolder YFP 2, and was sub-cloned from pSYFP2-C1  
560 (gift from Dorus Gadella (Addgene plasmid # 22878; <http://n2t.net/addgene:22878>;  
561 RRID:Addgene\_22878) (Kremers, Goedhart et al. 2006). All C-terminal repair templates were pooled,

562 purified using a PCR purification Kit (Blirt). Together with 10 µg Cas9 vector encoding the respective  
563 gRNA, 1 x 10<sup>7</sup> of freshly released RHΔku80DiCre tachyzoites (an improved version created by Dr  
564 Moritz Treeck from the original (Andenmatten, Egarter et al. 2013)) were transfected using 4D  
565 AMAXA electroporation. 24 hours after transfection, parasites were mechanically released, filtered  
566 and sorted for transient YFP expression into 96 well plates using a FACS sorter (FACSARIA III, BD  
567 Biosciences). Individual plaques were screened by PCR and the C-terminus of TgFRM2 was  
568 sequenced (Eurofins Genomics). Into a clone with TgFRM2-YFP-LoxP, the upstream LoxP was  
569 introduced as described. Screening for upstream LoxP integration was performed by PCR with a  
570 primer binding at the junction of gRNA binding sequence and LoxP site. Using a different set of  
571 primers, the complete upstream LoxP site was amplified via PCR and verified by sequencing. Two  
572 distinct clones were obtained for LoxPTgFRM2 (clone A and B) and used for phenotypic  
573 characterisation.

## 574 **12. Induction of the conditional TgFRM2 KO**

575 To obtain TgFRM2 KO parasites, the loxPTgFRM2-YFP parental line was grown in 50nM rapamycin  
576 containing media as described above until fixing. In IFA, TgFRM2 KO parasites were always compared  
577 to a control population of untreated loxPTgFRM2-YFP.

578 To quantify TgFRM2-YFP excision 48h post inoculation, 100 vacuoles were counted for each clone  
579 (clone A and B) and condition (RAP treated vs control population). The vacuoles were assessed with  
580 regards to their loss of FRM2-YFP signal. A single IFA was counted for each clone. To assess the  
581 apicoplast segregation phenotype in FRM2-YFP negative vacuoles, 66 (clone A) and 100 vacuoles  
582 (clone B) were counted. For this, quantification was achieved by using the same IFA that was used  
583 for the excision rate quantification.

## 584 **13. Transient transfection of CB-EME into *Toxoplasma* parasites**



585 To have parasites transiently expressing CB-EME, 1 x 10<sup>7</sup> of freshly released TgFRM2-HA or  
586 loxPTgFRM2-YFP parasites were transfected with 20 µg DNA by AMAXA electroporation.  
587 Subsequently, parasites were grown on HFFs as described above and fixed with 4%  
588 paraformaldehyde after 48h or 72h.

589 **Table T1. Antibodies used in this study**

Antibody	Reference
Anti actin	(Angrisano, Riglar et al. 2012), RRID: AB_2665920
Anti CPN60 (apicoplast)	(Agrawal, van Dooren et al. 2009)
Anti RON4	(Richard, MacRaidl et al. 2010)
Anti GAP45	(Jones, Kitson et al. 2006)
Anti MTIP	(Jones, Kitson et al. 2006)
Anti-enolase	(Dutta, Tewari et al. 2018)
Anti-HA	Roche (Cat #118743100)
Anti-YFP	Abcam (Cat #ab6556)
Anti-Atrx1	(DeRocher, Coppens et al. 2008)
Anti-G2Trx	Biddau and Sheiner, unpublished.

590

591 **Author contributions**

592 SD performed *P. falciparum* experiments. JFS performed *T. gondii* experiments. MS produced the  
593 TgFRM2-HA and LoxPTgFRM-YFP strains. JW performed bioinformatic analyses. SD and MM  
594 conceived the project. SD, MM and JFS wrote the manuscript.

595 **Acknowledgments**

596 We thank Prof. Mike Blackman for the kind gift of the PKG inhibitor Compound 2 and the B11 DiCre  
597 strain. We thank Dr. Jake Baum for the PFACT1 and RON4 antibodies, Dr. Julian Rayner for the MTIP  
598 and GAP45 antibodies, Dr Lilach Sheiner for the CPN60 and G2Trx antibodies, Prof Peter Bradley for  
599 the Atrx1 antibody and Prof GK Jarori for the enolase antibodies.

600 **Figure and Movie Legends**

601 **Figure 1, Chromobody constructs with different epitope tags label F-actin structures throughout**

602 **the *P. falciparum* lifecycle. A.** Chromobody constructs used in this study under the *hsp86* promoter  
603 with an emerald tag (CB-EME) and halo tag (CB-HALO). Blasticidin-S-deaminase (BSD) confers  
604 resistance to blasticidin. **B.** CB-EME and CB-HALO label actin filaments (DMSO), which disappear  
605 upon cytochalasin-D treatment (+CytoD). White arrows denote examples of F-actin structures. Also  
606 see **Video V3. C.** Super resolution imaging reveals an actin network in *P. falciparum* (CBEME), which  
607 stains partially similar to an actin antibody (actin). DAPI labels nuclei. See also **Fig. S1. D.** The F-actin  
608 network and dynamics can be visualised in gametocytes (see also **Video V5**). Brightfield images  
609 provided in greyscale alongside. Scale bar 5µm.

610 **Figure 2, Rapid actin dynamics are visible during intracellular growth, egress and invasion. A.**

611 Filopodia-like protrusions from the parasite cell body extend into the host cell cytosol (white  
612 arrows), which are disrupted by cytochalasin-D (+CytoD) and jasplakinolide (+JAS). **B.** Time lapse  
613 images show rapid changes in filopodia-like protrusions (white arrows). See also **Video V2.** CB-EME  
614 visible in the green channel, and brightfield images have been provided below in greyscale. **C.** Time  
615 lapse images show actin polymerising at a polar end of the merozoite, post egress (CB-EME).  
616 Corresponding brightfield images have been presented. Cytochalasin-D treatment prohibits the  
617 polar polymerisation of actin (+CytoD). **D.** IFA of invading merozoites with the junction marker RON4  
618 shows CB-EME staining close to the RON4 stain, implying that F-actin polymerises at the apical end  
619 prior to invasion.

620 **Figure 3, CB-EME staining of the F-actin network disappears upon genetic disruption of PfACT1: A.**

621 Schematic of transfection of CB-EME into the loxPpfact1 strain and PfACT1 loss upon DiCre-  
622 activation using rapamycin. **B.** The F-actin network (CB-EME, green and anti-PfACT1, red DMSO) is  
623 lost upon DiCre-mediated disruption of PfACT1 (RAP). DAPI labels nuclei. **C.** Giemsa-stained parasites  
624 showing invasion is abrogated in PfACT1 KOs. **D.** Live microscopy of CB-EME expressing parasites and

625 the loss of fluorescence intensity upon RAP-treatment. Right panel shows quantification of  
626 fluorescence intensities. **E.** Stills from live imaging of CB-EME expressing parasites co-stained with  
627 Mitotracker (mitochondria). The branched mitochondrial structure (DMSO) is not disrupted upon  
628 loss of PfACT1 (RAP). See also **Video V7**. **F.** IFA showing apicoplasts (red) colocalised with branches of  
629 the F-actin network (CB-EME, DMSO) and the disruption of the network together with apicoplasts  
630 when PfACT1 is deleted (RAP). Scale bar 5µm.

631 **Figure 4, Apicomplexan formins have distinct protein domains, with Formin-2 localising to**  
632 **apicoplasts in *Toxoplasma* and *P. falciparum*:** **A.** Other than the conserved FH1/FH2 domains, Pf/Tg  
633 Formin-1 contain tetratricopeptide repeat domains, while Pf/Tg Formin-2 contain a PTEN C2-like  
634 domain. **B.** Rooted neighbour-joining tree of FH2 domains detected in apicomplexan sequences  
635 flagged by hmmsearch and extracted from alignments produced by hmalign, both using the PFAM  
636 profile PF02181.23. Proteins with sub-sequences similar to PTEN-C2 domains (detected by psi-Blast)  
637 are indicated with circular leaf symbols (and shaded blue). Those sequences annotated as Formin-1  
638 (#) and Formin-2 (\*) are indicated. Colour coding of the leaf nodes: Red: Plasmodium, Green:  
639 Eimeria, Magenta: Sarcocystidae, Cyan: Piroplasmida, Black: Cryptosporidium, Grey: Gregarinidae **C.**  
640 Strategy depicting endogenous C-terminal HA tagging of TgFRM2 in *Toxoplasma*. CRISPR/Cas9 was  
641 exploited to introduce a double-stranded DNA break and repair DNA amplified by PCR with  
642 homologous DNA regions coding for 3xHA. **D.** Diagnostic PCR confirming integration of DNA  
643 described in C into the RH\_Δku80\_DiCre line. **E.** IFA showing localisation of TgFRM2-HA (green) at  
644 the vicinity of the apicoplast staining (anti-G2Trx, red). Nuclei are stained with DAPI (blue). White  
645 dotted line depicts the parasite vacuole outline. *Toxoplasma* parasites were fixed 24h after  
646 inoculation. **F.** Super-resolution microscopy confirming the close apposition of TgFRM2-HA (green)  
647 to the apicoplast (anti-G2Trx, orange). *Toxoplasma* parasites were fixed 24h after inoculation. Scale  
648 bar is 2.5µm. **G.** Strategy showing simultaneous floxing and C-terminal HA tagging of the *pfformin2*  
649 locus using single cross over recombination into a DiCre expressing strain to give rise to the  
650 LoxPpfformin2 strain (modified). Primers for diagnostic PCR have been annotated as half arrows. **H.**

651 Diagnostic PCR confirming integration in one of the two transfected lines (integrant). **I.** IFA showing  
652 localisation of PffRM2-HA (green) in the context of a PFACT1-antibody staining (red). Nuclei are  
653 stained with DAPI (blue). **J.** IFA showing localisation of PffRM2-HA adjacent to the apicoplast using a  
654 CPN60 antibody (red) throughout *P. falciparum* intracellular development (20, 40, 48h). **K.** Super-  
655 resolution image confirming the tight apposition of PffRM2 (green) with apicoplasts (orange). Scale  
656 bars are 5µm, except where stated otherwise.

657 **Figure 5, Conditional deletion of PffRM2 disrupts apicoplast segregation and causes a severe**  
658 **fitness defect: A.** Strategy showing the DiCre-mediated genomic excision of the LoxPpffRM2 locus.  
659 Primers for diagnostic PCR have been annotated as red/blue half arrows. **B.** Diagnostic PCR  
660 confirming genomic excision of the *pffrm2* locus upon rapamycin treatment (+). **C.** A growth curve  
661 showing the relative fitness of RAP-treated PffRM2 KO parasites in comparison to DMSO controls.  
662 Various time points from the pulse treatment of 1h-old rings at time 0 in the 1<sup>st</sup>, 2<sup>nd</sup> and 3<sup>rd</sup> growth  
663 cycles have been measured. **D.** left panel, Western blot showing the loss of PffRM2-HA upon RAP-  
664 treatment, enolase has been used as a control. Right panel, Quantification of PffRM2-HA from three  
665 different blots shows at least a 10-fold drop in protein levels, Error bars depict SD. **E.** IFA showing  
666 loss of PffRM2-HA staining (green) upon RAP-treatment. Levels of PFACT1-staining (red) do not  
667 change. **F.** Giemsa stained images of RAP-treated parasites reveal dysmorphic parasites. **G.**  
668 Apicoplast segregation (red) is affected to various degrees in RAP-treated parasites as compared to  
669 DMSO controls. See also **Figs. S3A** and **6D**. **H.** Quantification of phenotypes seen in **G**. Error bars  
670 depict SD. **I.** Isopentenyl pyrophosphate (IPP) cannot rescue the fitness defect (RAP+IPP) in PffRM2  
671 KO parasites (RAP) as compared to parasitemia to the DMSO controls. Error bars depict SD. Scale  
672 bars 5 µm.

673 **Figure 6, Conditional deletion of PffRM2 abrogates the intracellular F-actin network but not the**  
674 **apical polymerisation of F-actin prior to invasion: A.** Strategy showing episomal expression of CB-  
675 EME in the LoxPpffrm2 background. **B.** Upper panels: Stills from a video showing loss of normal

676 intracellular F-actin fluorescence (green). Brightfield images have been provided. See also **Video V8**.  
677 Lower left panel: Zoomed images of indicated parasites in upper panels showing loss of the actin  
678 network in RAP (none, red arrows) as compared to DMSO controls (normal). **C.** Graph showing loss  
679 of normal F-actin fluorescence in ~95% RAP-treated parasites. >90% of DMSO controls show  
680 presence of the network. **D.** IFA staining of the apicoplast with a CPN60 antibody (red) on top of the  
681 fluorescent F-actin network (green) shows a defect in apicoplast segregation in RAP treated  
682 parasites (white arrows). Nuclei are stained in blue and brightfield images are provided alongside.  
683 Examples of normally segregated apicoplasts, intermediate and severely disrupted apicoplasts have  
684 been provided. **E.** Loss of filopodia in RAP-treated young trophozoites imaged 72h post-RAP  
685 treatment. Stills from a video have been shown, where time points are depicted in white. Normal  
686 filopodia are marked with white arrows in DMSO controls. **F.** Post-schizont egress, merozoites from  
687 DMSO controls and RAP-treated group show similar propensity to polymerise apical F-actin (CB-EME  
688 fluorescence shown in green). Red arrows show apical F-actin in zoomed images (lower panels).  
689 Scale bars 5 $\mu$ m.

690 **Figure 7. Conditional deletion of TgFRM2 disrupts normal segregation of apicoplasts together with**  
691 **abrogation of the intracellular F-actin polymerisation centre. A.** Strategy to generate LoxPTgFRM2-  
692 YFP, a floxed and C-terminal YFP-tagged *TgFRM2* locus in the RH\_Δku80\_DiCre line. For this purpose,  
693 CRISPR/Cas9 was exploited to introduce DNA double-strand breaks in the 5' UTR and C-terminus of  
694 the *TgFRM2* gene. Integration was confirmed by PCR (see **Fig. S5A**). Arrows represent PCR primers  
695 used in **Fig. S5A**. **B.** IFA staining with anti-YFP (TgFRM2-YFP) and anti-Atrx1 (apicoplast) shows an  
696 apicoplast segregation defect in TgFRM2-YFP KO parasites. In control parasites, TgFRM2-YFP  
697 localises to the vicinity of the apicoplast (upper panel). The loss of TgFRM2-YFP causes an apicoplast  
698 segregation defect (lower panel, white arrow). The lower panel depicts a TgFRM2-YFP KO vacuole  
699 together with a TgFRM2-YFP positive vacuole for comparison. Scale bars are 5 $\mu$ m. **C.** IFA depicting  
700 CB-EME and apicoplast (anti-CPN60) in control and RAP-treated LoxPTgFRM2-YFP parasites. In  
701 untreated parasites, the apicoplast localises to intracellular actin polymerisation centres (control,

702 white arrows in zoom). Parasites exhibiting TgFRM2 KO-specific apicoplast phenotype lack  
703 intracellular actin polymerisation centres. Zoomed images depict indicted areas. Scale bars are 5µm.  
704 IFAs depicted in this figure were performed for the LoxPTgFRM2 clone B.

705 **Figure 8. A model showing the dependence of apicoplast segregation on the intracellular F-actin**  
706 **network in *P. falciparum* and *Toxoplasma*.** In apicomplexan parasites, despite using different  
707 replication modes (endodyogeny, schizogony), the function of actin and Formin-2 is highly conserved  
708 with regards to intracellular F-actin dynamics and apicoplast inheritance. One difference appears to  
709 be the formation of an intravacuolar network that can still occur in the case of *T.gondii* but not *P.*  
710 *falciparum* upon disruption of Formin-2.

711 **Figure S1, Super-resolution of the CB-EME-labelled F-actin network: A.** Super-resolution imaging of  
712 schizonts show the F-actin network (CB-EME, yellow) co-stained in magenta with IMC-markers  
713 GAP45, MTIP and the apicoplast marker CPN60. Note the very close apposition of the apicoplasts  
714 with the F-actin network. DAPI stains nuclei (cyan). **B.** Mean fluorescence intensity of the CB-EME  
715 channel of each of the schizonts has been presented, N=40. Error bars show SD.

716 **Figure S2: CB-HALO labels the F-actin network similar to CB-EME. A.** IFA of CB-HALO expressing  
717 parasites showing staining with anti-PfACT1 and with an anti-HALO antibody. Note that the anti-  
718 HALO antibody shows background staining in the parental strain. **B.** Intensity of CB-HALO expression  
719 and filament structures (red) are lost upon PfACT1 disruption (RAP). **C.** IFA with anti-GAP45  
720 antibodies show normal formation of merozoites in PfACT1-disrupted parasites (RAP) expressing CB-  
721 HALO.

722 **Figure S3. Additional defects in merozoite formation/ cytokinesis in PfFRM2 KO parasites. A.** IFA  
723 image showing schizonts with varying degrees of apicoplast (red) segregation defect 44h post-RAP-  
724 treatment of LoxPpffrm2. An example of an intermediate apicoplast defect has been shown (white  
725 arrow). Nuclei are stained in blue. **B.** Number of nuclei in the IFA from A were binned to <5, 5 to 16

726 and 16+ in DMSO controls and RAP-treated parasites. The graph shows a general reduction in the  
727 number of nuclei in RAP-treated parasites. **C.** LoxPpffrm2/CBEME parasites were stained with an  
728 anti-GAP45 antibody (red) 44h post DMSO/RAP-treatment and examples of the IMC defect have  
729 been provided. CBEME fluorescence is shown in green. **D.** Upon quantification of C, normally formed  
730 merozoites reduced significantly in PffRM2 KOs. **E.** When DMSO/RAP-treated schizonts were  
731 allowed to egress, conjoined merozoites were apparent in the RAP treated controls (red arrows) but  
732 not in DMSO controls.

733 **Figure S4. Formin-2 localises to the F-actin network in *P. falciparum* and *T.gondii*: Upper panel.** IFA  
734 depicting PffRM2-HA localisation using an anti-HA antibody in *P. falciparum* expressing CB-EME  
735 (green). PffRM2-HA localises to F-actin (merge, white arrows). Nuclei were stained with DAPI (blue).  
736 **Lower panel.** IFA showing staining for TgFRM2-HA using an anti-HA antibody in *Toxoplasma*  
737 transiently expressing CB-EME (green). TgFRM2-HA localised in close proximity to intracellular actin  
738 polymerisation events (merge, white arrows). Parasites were transiently transfected with CB-EME  
739 and grown for 48h. Scale bars are 5µm.

#### 740 **Figure S5. Loss of TgFRM2-YFP upon RAP-treatment**

741 **A.** Integration PCR for TgFRM2-YFP parasites described in **Fig. 7** confirming 5' integration (i) and 3'  
742 integration (ii). While the amplification of YFP indicates the presence of non-induced parasites in the  
743 rapamycin-treated population (iii), excision of TgFRM2-YFP could only be shown for parasites  
744 growing under rapamycin (iv). For the excision PCRs (iii, iv) parasites were grown with or without  
745 50nM Rapamycin and mechanically lysed after 48h prior to gDNA collection. Coloured arrows refer  
746 to **Fig. 7A** and indicate the sequence amplified by PCR. **B.** IFA depicting apicoplast (anti-CPN60) and  
747 background fluorescence in LoxPTgFRM2-YFP parasites (clone B), which outlines the mitochondria.  
748 In the control population (without rapamycin treatment), the YFP-tagged FRM2 was not detectable  
749 in the absence of an YFP-antibody. RAP-treated parasites show the characteristic mislocalisation of

750 apicoplast material into the residual body, while mitochondria appear unaffected. Parasites were  
751 grown for 72h before fixation. Scale bars are 5 $\mu$ m.

752 **Movie V1, Rapid shape changes of ring stages of *P. falciparum* expressing CB-EME (green).**

753 Acquisition time is shown in seconds. Scale bar 5 $\mu$ m.

754 **Movie V2, Dynamic Filopodia-like F-actin extensions from the parasite edges into the RBC cytosol.**

755 Acquisition time is shown in seconds. Scale bar 5 $\mu$ m.

756 **Movie V3, Dynamic actin filaments in CB-EME expressing parasites (DMSO) are disrupted upon**

757 **addition of cytochalasin-D.** The green channel shows CB-EME expression. Brightfield images also

758 shown. Acquisition time is shown in seconds. Scale bar 5 $\mu$ m.

759 **Movie V4, Polar polymerisation of F-actin at the merozoite tip following egress.** Time lapse images

760 of a representative schizont which undergoes egress, followed by polymerisation of F-actin at the

761 merozoite edge (white arrows appearing). Images (green channel, CBEME) and brightfield

762 (greyscale) were acquired every 5 sec. Acquisition time is shown in seconds. Scale bar 5 $\mu$ m.

763 **Movie V5, F-actin dynamics in gametocytes.** Two representative examples of gametocytes

764 expressing CB-EME show dynamic filaments running along the parasite length and enriched at the

765 tips. Acquisition time is shown in seconds. Scale bar 5 $\mu$ m.

766 **Movie V6, Multilobular structures of trophozoites are not lost upon addition of cytochalasin-D.**

767 **Movie V7, CB-EME staining disappears upon conditional genetic deletion of *pfact1*.** Ring stage

768 LoxPpfACT1/CBEME parasites were pulse treated with DMSO or RAP for 4h and imaged after 40

769 hours. CB-EME was imaged in the green channel and shows a disappearance of F-actin upon RAP-

770 treatment. Mitochondria were stained with Mitotracker<sup>®</sup> (red channel). Acquisition time is shown in

771 seconds. Scale bar 5 $\mu$ m.



772 **Movie V8, Actin filaments disappear upon genetic deletion of *pffrm2*.** Ring stage  
773 LoxPpffRM2/CBEME parasites were DMSO- or RAP-treated for 4h and imaged 40 hours later. CB-  
774 EME was imaged in the green channel and shows a disappearance of intracellular F-actin upon RAP-  
775 treatment. Acquisition time is shown in seconds. Scale bar 5µm.

## 776 Citations

777 Agrawal, S., G. G. van Dooren, W. L. Beatty and B. Striepen (2009). "Genetic evidence that an  
778 endosymbiont-derived endoplasmic reticulum-associated protein degradation (ERAD) system  
779 functions in import of apicoplast proteins." J Biol Chem **284**(48): 33683-33691.

780 Andenmatten, N., S. Egarter, A. J. Jackson, N. Jullien, J. P. Herman and M. Meissner (2013).  
781 "Conditional genome engineering in *Toxoplasma gondii* uncovers alternative invasion mechanisms."  
782 Nat Methods **10**(2): 125-127.

783 Angrisano, F., D. T. Riglar, A. Sturm, J. C. Volz, M. J. Delves, E. S. Zuccala, L. Turnbull, C. Dekiwadia, M.  
784 A. Olshina, D. S. Marapana, W. Wong, V. Mollard, C. H. Bradin, C. J. Tonkin, P. W. Gunning, S. A.  
785 Ralph, C. B. Whitchurch, R. E. Sinden, A. F. Cowman, G. I. McFadden and J. Baum (2012). "Spatial  
786 localisation of actin filaments across developmental stages of the malaria parasite." PLoS One **7**(2):  
787 e32188.

788 Baker, D. A., L. G. Drought, C. Flueck, S. D. Nofal, A. Patel, M. Penzo and E. M. Walker (2017). "Cyclic  
789 nucleotide signalling in malaria parasites." Open Biol **7**(12).

790 Bannister, L. H., J. M. Hopkins, R. E. Fowler, S. Krishna and G. H. Mitchell (2000). "A brief illustrated  
791 guide to the ultrastructure of *Plasmodium falciparum* asexual blood stages." Parasitol Today **16**(10):  
792 427-433.

793 Baum, J., T. W. Gilberger, F. Frischknecht and M. Meissner (2008). "Host-cell invasion by malaria  
794 parasites: insights from *Plasmodium* and *Toxoplasma*." Trends Parasitol **24**(12): 557-563.

795 Baum, J., A. T. Papenfuss, B. Baum, T. P. Speed and A. F. Cowman (2006). "Regulation of  
796 apicomplexan actin-based motility." Nat Rev Microbiol **4**(8): 621-628.

797 Baum, J., C. J. Tonkin, A. S. Paul, M. Rug, B. J. Smith, S. B. Gould, D. Richard, T. D. Pollard and A. F.  
798 Cowman (2008). "A malaria parasite formin regulates actin polymerization and localizes to the  
799 parasite-erythrocyte moving junction during invasion." Cell Host Microbe **3**(3): 188-198.

800 Blackman, M. J. (1994). "Purification of *Plasmodium falciparum* merozoites for analysis of the  
801 processing of merozoite surface protein-1." Methods Cell Biol **45**: 213-220.

802 Collins, C. R., S. Das, E. H. Wong, N. Andenmatten, R. Stallmach, F. Hackett, J. P. Herman, S. Muller,  
803 M. Meissner and M. J. Blackman (2013). "Robust inducible Cre recombinase activity in the human  
804 malaria parasite *Plasmodium falciparum* enables efficient gene deletion within a single asexual  
805 erythrocytic growth cycle." Mol Microbiol **88**(4): 687-701.

- 806 Collins, C. R., F. Hackett, M. Strath, M. Penzo, C. Withers-Martinez, D. A. Baker and M. J. Blackman  
807 (2013). "Malaria parasite cGMP-dependent protein kinase regulates blood stage merozoite secretory  
808 organelle discharge and egress." PLoS Pathog **9**(5): e1003344.
- 809 Courtemanche, N. (2018). "Mechanisms of formin-mediated actin assembly and dynamics." Biophys  
810 Rev.
- 811 Crabb, B. S. and A. F. Cowman (1996). "Characterization of promoters and stable transfection by  
812 homologous and nonhomologous recombination in Plasmodium falciparum." Proc Natl Acad Sci U S  
813 A **93**(14): 7289-7294.
- 814 Curt-Varesano, A., L. Braun, C. Ranquet, M. A. Hakimi and A. Bougdour (2016). "The aspartyl  
815 protease TgASP5 mediates the export of the Toxoplasma GRA16 and GRA24 effectors into host  
816 cells." Cell Microbiol **18**(2): 151-167.
- 817 Daher, W., N. Klages, M. F. Carlier and D. Soldati-Favre (2012). "Molecular characterization of  
818 Toxoplasma gondii formin 3, an actin nucleator dispensable for tachyzoite growth and motility."  
819 Eukaryot Cell **11**(3): 343-352.
- 820 Daher, W., F. Plattner, M. F. Carlier and D. Soldati-Favre (2010). "Concerted action of two formins in  
821 gliding motility and host cell invasion by Toxoplasma gondii." PLoS Pathog **6**(10): e1001132.
- 822 Das, S., J. E. Dixon and W. Cho (2003). "Membrane-binding and activation mechanism of PTEN." Proc  
823 Natl Acad Sci U S A **100**(13): 7491-7496.
- 824 Das, S., N. Hertrich, A. J. Perrin, C. Withers-Martinez, C. R. Collins, M. L. Jones, J. M. Watermeyer, E.  
825 T. Fobes, S. R. Martin, H. R. Saibil, G. J. Wright, M. Treeck, C. Epp and M. J. Blackman (2015).  
826 "Processing of Plasmodium falciparum Merozoite Surface Protein MSP1 Activates a Spectrin-Binding  
827 Function Enabling Parasite Egress from RBCs." Cell Host Microbe **18**(4): 433-444.
- 828 Das, S., L. Lemgruber, C. L. Tay, J. Baum and M. Meissner (2017). "Multiple essential functions of  
829 Plasmodium falciparum actin-1 during malaria blood-stage development." BMC Biol **15**(1): 70.
- 830 DeRocher, A. E., I. Coppens, A. Karnataki, L. A. Gilbert, M. E. Rome, J. E. Feagin, P. J. Bradley and M.  
831 Parsons (2008). "A thioredoxin family protein of the apicoplast periphery identifies abundant  
832 candidate transport vesicles in Toxoplasma gondii." Eukaryot Cell **7**(9): 1518-1529.
- 833 Douglas, R. G., P. Nandekar, J. E. Aktories, H. Kumar, R. Weber, J. M. Sattler, M. Singer, S. Lepper, S.  
834 K. Sadiq, R. C. Wade and F. Frischknecht (2018). "Inter-subunit interactions drive divergent dynamics  
835 in mammalian and Plasmodium actin filaments." PLoS Biol **16**(7): e2005345.
- 836 Dutta, S., A. Tewari, C. Balaji, R. Verma, A. Moitra, M. Yadav, P. Agrawal, D. Sahal and G. K. Jarori  
837 (2018). "Strain-transcending neutralization of malaria parasite by antibodies against Plasmodium  
838 falciparum enolase." Malar J **17**(1): 304.
- 839 Edgar, R. C. (2004). "MUSCLE: multiple sequence alignment with high accuracy and high  
840 throughput." Nucleic Acids Res **32**(5): 1792-1797.
- 841 Egarter, S., N. Andenmatten, A. J. Jackson, J. A. Whitelaw, G. Pall, J. A. Black, D. J. Ferguson, I.  
842 Tardieux, A. Mogilner and M. Meissner (2014). "The toxoplasma Acto-MyoA motor complex is  
843 important but not essential for gliding motility and host cell invasion." PLoS One **9**(3): e91819.

- 844 El-Gebali, S., J. Mistry, A. Bateman, S. R. Eddy, A. Luciani, S. C. Potter, M. Qureshi, L. J. Richardson, G.  
845 A. Salazar, A. Smart, E. L. L. Sonnhammer, L. Hirsh, L. Paladin, D. Piovesan, S. C. E. Tosatto and R. D.  
846 Finn (2018). "The Pfam protein families database in 2019." Nucleic Acids Res.
- 847 Francia, M. E. and B. Striepen (2014). "Cell division in apicomplexan parasites." Nat Rev Microbiol  
848 **12**(2): 125-136.
- 849 Frenal, K., J. F. Dubremetz, M. Lebrun and D. Soldati-Favre (2017). "Gliding motility powers invasion  
850 and egress in Apicomplexa." Nat Rev Microbiol **15**(11): 645-660.
- 851 Gardner, M. J., N. Hall, E. Fung, O. White, M. Berriman, R. W. Hyman, J. M. Carlton, A. Pain, K. E.  
852 Nelson, S. Bowman, I. T. Paulsen, K. James, J. A. Eisen, K. Rutherford, S. L. Salzberg, A. Craig, S. Kyes,  
853 M. S. Chan, V. Nene, S. J. Shallom, B. Suh, J. Peterson, S. Angiuoli, M. Pertea, J. Allen, J. Selengut, D.  
854 Haft, M. W. Mather, A. B. Vaidya, D. M. Martin, A. H. Fairlamb, M. J. Fraunholz, D. S. Roos, S. A.  
855 Ralph, G. I. McFadden, L. M. Cummings, G. M. Subramanian, C. Mungall, J. C. Venter, D. J. Carucci, S.  
856 L. Hoffman, C. Newbold, R. W. Davis, C. M. Fraser and B. Barrell (2002). "Genome sequence of the  
857 human malaria parasite *Plasmodium falciparum*." Nature **419**(6906): 498-511.
- 858 Gruring, C., A. Heiber, F. Kruse, J. Ungefehr, T. W. Gilberger and T. Spielmann (2011). "Development  
859 and host cell modifications of *Plasmodium falciparum* blood stages in four dimensions." Nat  
860 Commun **2**: 165.
- 861 Hliscs, M., C. Millet, M. W. Dixon, I. Siden-Kiamos, P. McMillan and L. Tilley (2015). "Organization and  
862 function of an actin cytoskeleton in *Plasmodium falciparum* gametocytes." Cell Microbiol **17**(2): 207-  
863 225.
- 864 Jacot, D., W. Daher and D. Soldati-Favre (2013). "Toxoplasma gondii myosin F, an essential motor for  
865 centrosomes positioning and apicoplast inheritance." EMBO J **32**(12): 1702-1716.
- 866 Jones, M. L., S. Das, H. Belda, C. R. Collins, M. J. Blackman and M. Treeck (2016). "A versatile strategy  
867 for rapid conditional genome engineering using loxP sites in a small synthetic intron in *Plasmodium*  
868 *falciparum*." Sci Rep **6**: 21800.
- 869 Jones, M. L., E. L. Kitson and J. C. Rayner (2006). "*Plasmodium falciparum* erythrocyte invasion: a  
870 conserved myosin associated complex." Mol Biochem Parasitol **147**(1): 74-84.
- 871 Keller, O., M. Kollmar, M. Stanke and S. Waack (2011). "A novel hybrid gene prediction method  
872 employing protein multiple sequence alignments." Bioinformatics **27**(6): 757-763.
- 873 Kremers, G. J., J. Goedhart, E. B. van Munster and T. W. Gadella, Jr. (2006). "Cyan and yellow super  
874 fluorescent proteins with improved brightness, protein folding, and FRET Forster radius."  
875 Biochemistry **45**(21): 6570-6580.
- 876 Kumar, S., M. Kumar, R. Ekka, J. D. Dvorin, A. S. Paul, A. K. Madugundu, T. Gilberger, H. Gowda, M. T.  
877 Duraisingh, T. S. Keshava Prasad and P. Sharma (2017). "PfCDPK1 mediated signaling in erythrocytic  
878 stages of *Plasmodium falciparum*." Nat Commun **8**(1): 63.
- 879 Kumpula, E. P. and I. Kursula (2015). "Towards a molecular understanding of the apicomplexan actin  
880 motor: on a road to novel targets for malaria remedies?" Acta Crystallogr F Struct Biol Commun  
881 **71**(Pt 5): 500-513.
- 882 Melak, M., M. Plessner and R. Grosse (2017). "Actin visualization at a glance." J Cell Sci **130**(3): 525-  
883 530.

- 884 Panza, P., J. Maier, C. Schmees, U. Rothbauer and C. Sollner (2015). "Live imaging of endogenous  
885 protein dynamics in zebrafish using chromobodies." *Development* **142**(10): 1879-1884.
- 886 Periz, J., J. Whitelaw, C. Harding, S. Gras, M. I. Del Rosario Minina, F. Latorre-Barragan, L. Lemgruber,  
887 M. A. Reimer, R. Insall, A. Heaslip and M. Meissner (2017). "Toxoplasma gondii F-actin forms an  
888 extensive filamentous network required for material exchange and parasite maturation." *Elife* **6**.
- 889 Perrin, A. J., C. R. Collins, M. R. G. Russell, L. M. Collinson, D. A. Baker and M. J. Blackman (2018).  
890 "The Actinomyosin Motor Drives Malaria Parasite Red Blood Cell Invasion but Not Egress." *MBio*  
891 **9**(4).
- 892 Richard, D., C. A. MacRaild, D. T. Riglar, J. A. Chan, M. Foley, J. Baum, S. A. Ralph, R. S. Norton and A.  
893 F. Cowman (2010). "Interaction between Plasmodium falciparum apical membrane antigen 1 and the  
894 rhoptry neck protein complex defines a key step in the erythrocyte invasion process of malaria  
895 parasites." *J Biol Chem* **285**(19): 14815-14822.
- 896 Riglar, D. T., D. Richard, D. W. Wilson, M. J. Boyle, C. Dekiwadia, L. Turnbull, F. Angrisano, D. S.  
897 Marapana, K. L. Rogers, C. B. Whitchurch, J. G. Beeson, A. F. Cowman, S. A. Ralph and J. Baum (2011).  
898 "Super-resolution dissection of coordinated events during malaria parasite invasion of the human  
899 erythrocyte." *Cell Host Microbe* **9**(1): 9-20.
- 900 Rocchetti, A., C. Hawes and V. Kriechbaumer (2014). "Fluorescent labelling of the actin cytoskeleton  
901 in plants using a cameloid antibody." *Plant Methods* **10**: 12.
- 902 Schuler, H. and K. Matuschewski (2006). "Regulation of apicomplexan microfilament dynamics by a  
903 minimal set of actin-binding proteins." *Traffic* **7**(11): 1433-1439.
- 904 Soldati, D., B. J. Foth and A. F. Cowman (2004). "Molecular and functional aspects of parasite  
905 invasion." *Trends Parasitol* **20**(12): 567-574.
- 906 Svitkina, T. M. (2018). "Ultrastructure of the actin cytoskeleton." *Curr Opin Cell Biol* **54**: 1-8.
- 907 Tardieux, I. (2017). "Actin Nanobodies Uncover the Mystery of Actin Filament Dynamics in  
908 Toxoplasma gondii." *Trends Parasitol*.
- 909 Tardieux, I. (2017). "Actin Nanobodies Uncover the Mystery of Actin Filament Dynamics in  
910 Toxoplasma gondii." *Trends Parasitol* **33**(8): 579-581.
- 911 Thomas, J. A., C. R. Collins, S. Das, F. Hackett, A. Graindorge, D. Bell, E. Deu and M. J. Blackman  
912 (2016). "Development and Application of a Simple Plaque Assay for the Human Malaria Parasite  
913 Plasmodium falciparum." *PLoS One* **11**(6): e0157873.
- 914 Thompson, J. D., D. G. Higgins and T. J. Gibson (1994). "CLUSTAL W: improving the sensitivity of  
915 progressive multiple sequence alignment through sequence weighting, position-specific gap  
916 penalties and weight matrix choice." *Nucleic Acids Res* **22**(22): 4673-4680.
- 917 Torgerson, P. R. and P. Mastroiacovo (2013). "The global burden of congenital toxoplasmosis: a  
918 systematic review." *Bull World Health Organ* **91**(7): 501-508.
- 919 Vahokoski, J., S. P. Bhargav, A. Desfosses, M. Andreadaki, E. P. Kumpula, S. M. Martinez, A. Ignatev,  
920 S. Lepper, F. Frischknecht, I. Siden-Kiamos, C. Sachse and I. Kursula (2014). "Structural differences  
921 explain diverse functions of Plasmodium actins." *PLoS Pathog* **10**(4): e1004091.

- 922 Weiss, G. E., P. R. Gilson, T. Taechalertpaisarn, W. H. Tham, N. W. de Jong, K. L. Harvey, F. J. Fowkes,  
923 P. N. Barlow, J. C. Rayner, G. J. Wright, A. F. Cowman and B. S. Crabb (2015). "Revealing the  
924 sequence and resulting cellular morphology of receptor-ligand interactions during *Plasmodium*  
925 *falciparum* invasion of erythrocytes." *PLoS Pathog* **11**(2): e1004670.
- 926 White, N. J., S. Pukrittayakamee, T. T. Hien, M. A. Faiz, O. A. Mokuolu and A. M. Dondorp (2014).  
927 "Malaria." *Lancet* **383**(9918): 723-735.
- 928 Whitelaw, J. A., F. Latorre-Barragan, S. Gras, G. S. Pall, J. M. Leung, A. Heaslip, S. Egarter, N.  
929 Andenmatten, S. R. Nelson, D. M. Warshaw, G. E. Ward and M. Meissner (2017). "Surface  
930 attachment, promoted by the actomyosin system of *Toxoplasma gondii* is important for efficient  
931 gliding motility and invasion." *BMC Biol* **15**(1): 1.
- 932 Yeh, E. and J. L. DeRisi (2011). "Chemical rescue of malaria parasites lacking an apicoplast defines  
933 organelle function in blood-stage *Plasmodium falciparum*." *PLoS Biol* **9**(8): e1001138.
- 934 Zhang, Z., Y. Zhang, H. Tan, Y. Wang, G. Li, W. Liang, Z. Yuan, J. Hu, H. Ren and D. Zhang (2011). "RICE  
935 MORPHOLOGY DETERMINANT encodes the type II formin FH5 and regulates rice morphogenesis."  
936 *Plant Cell* **23**(2): 681-700.
- 937

# Figure 1

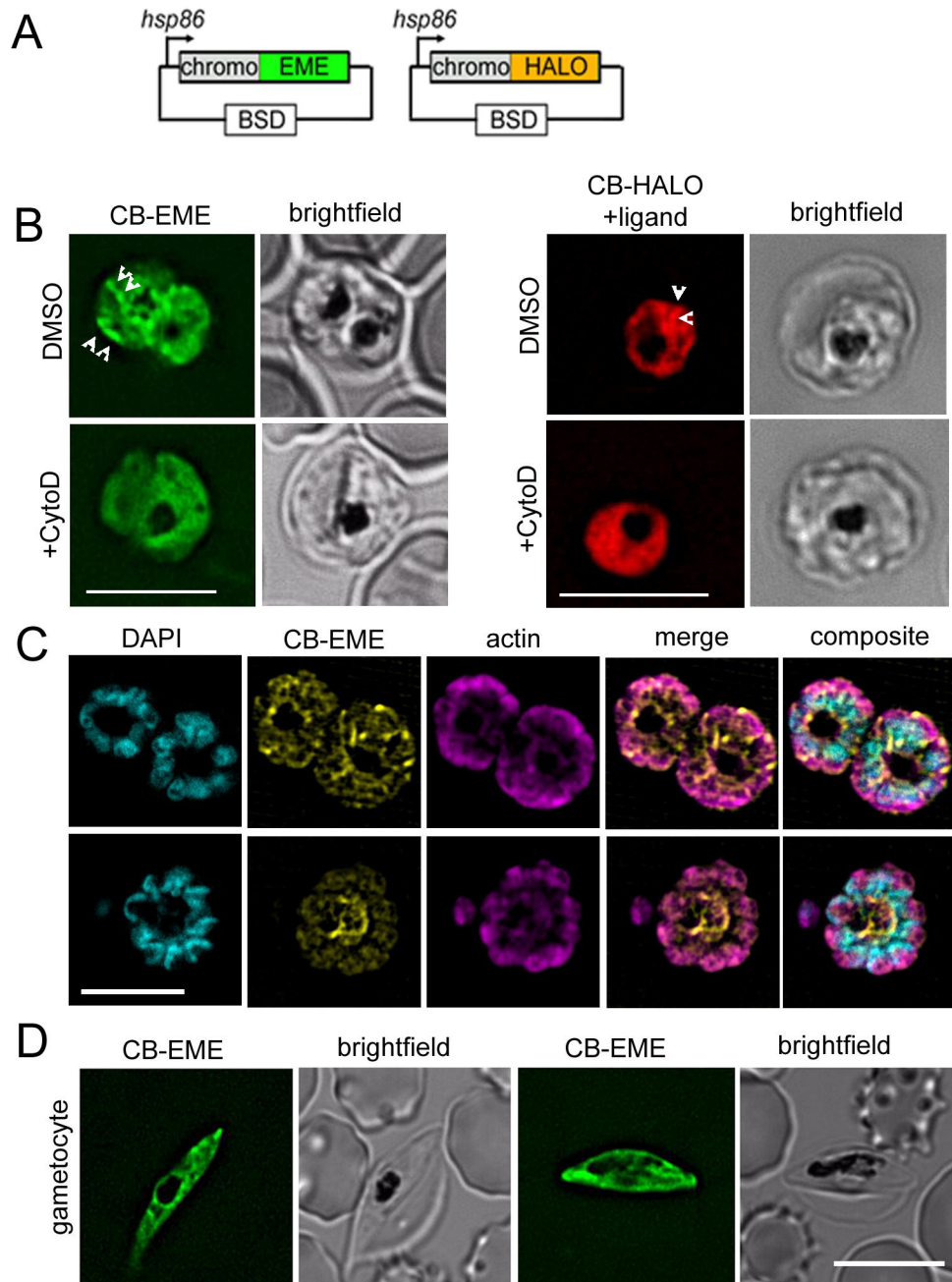
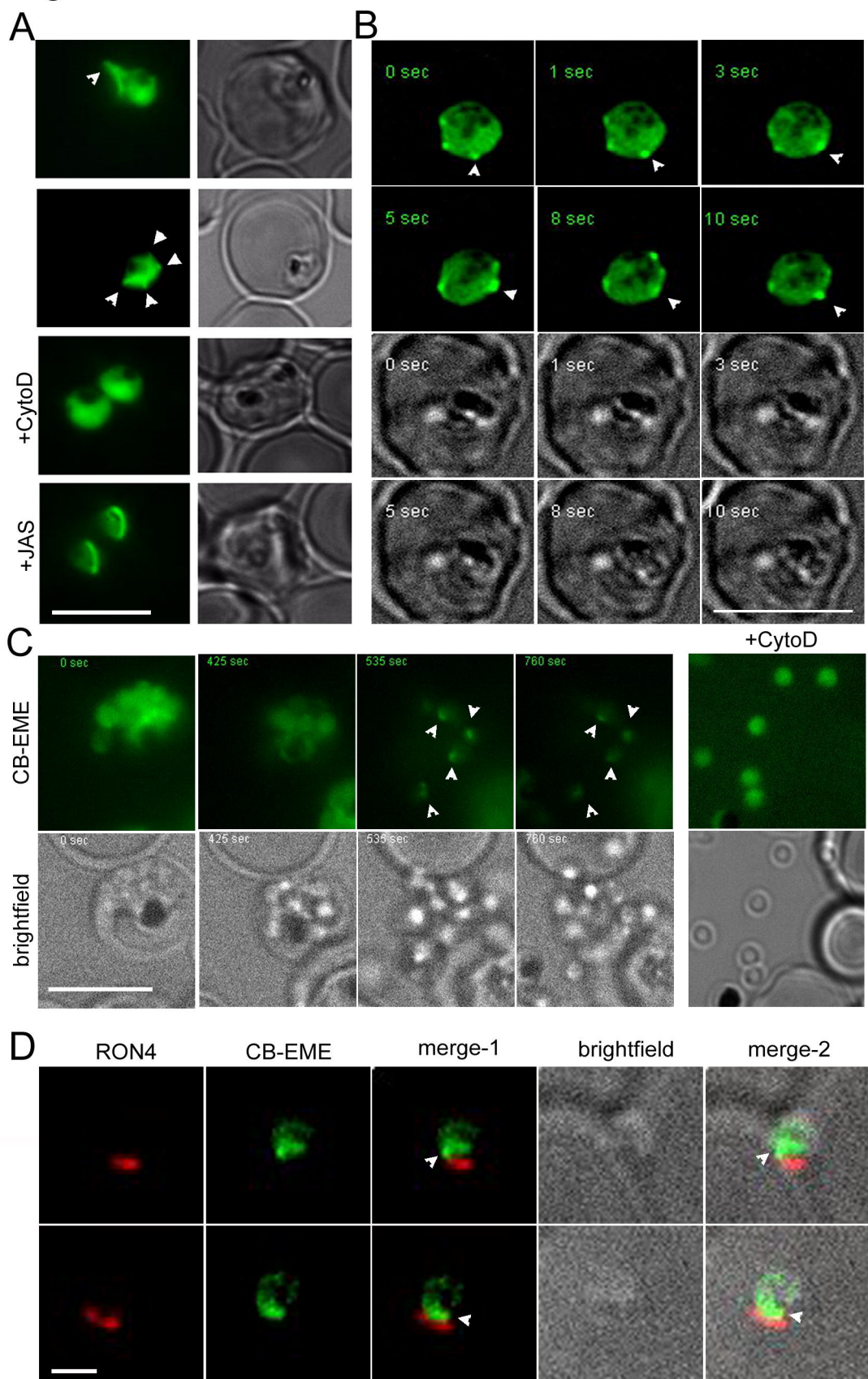
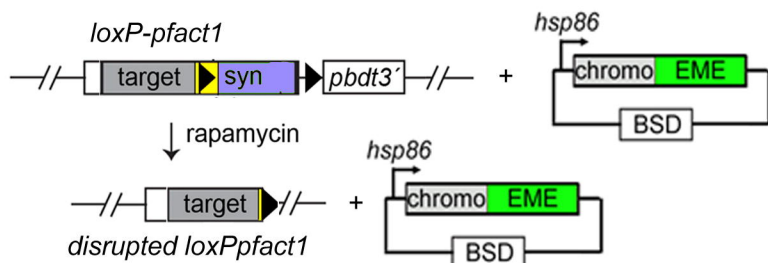
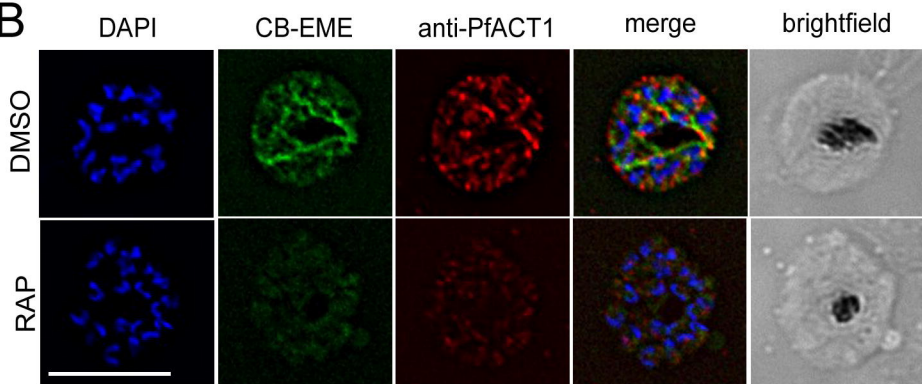
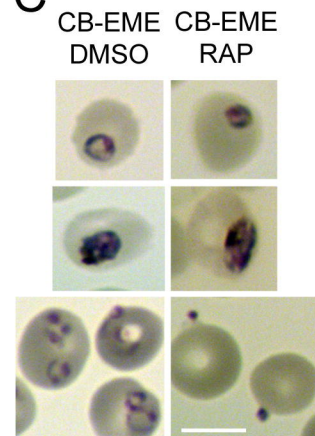
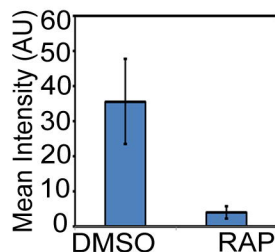
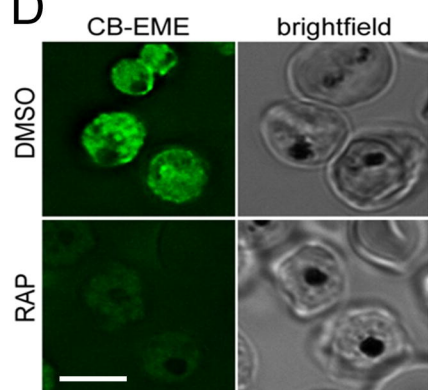
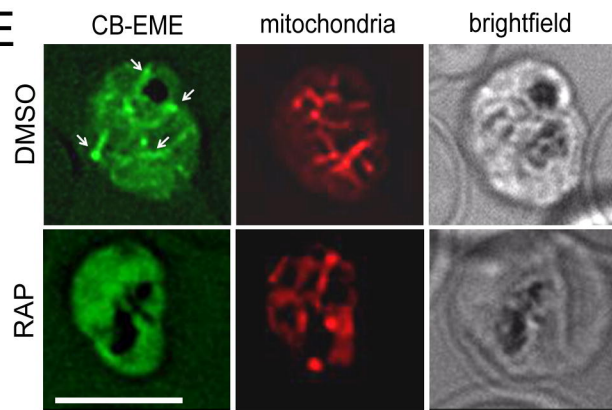
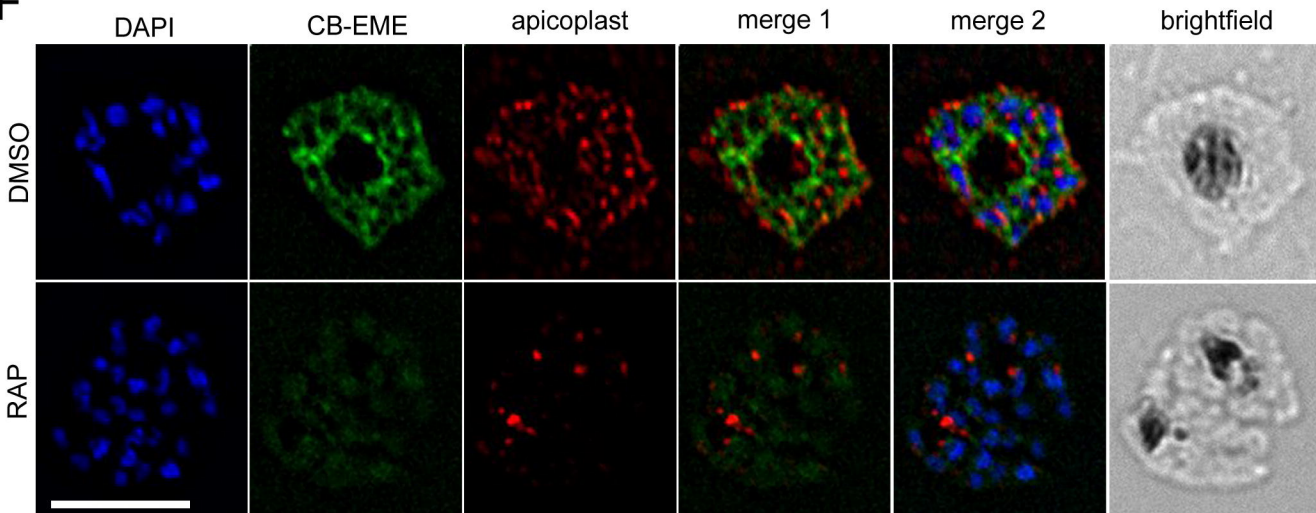


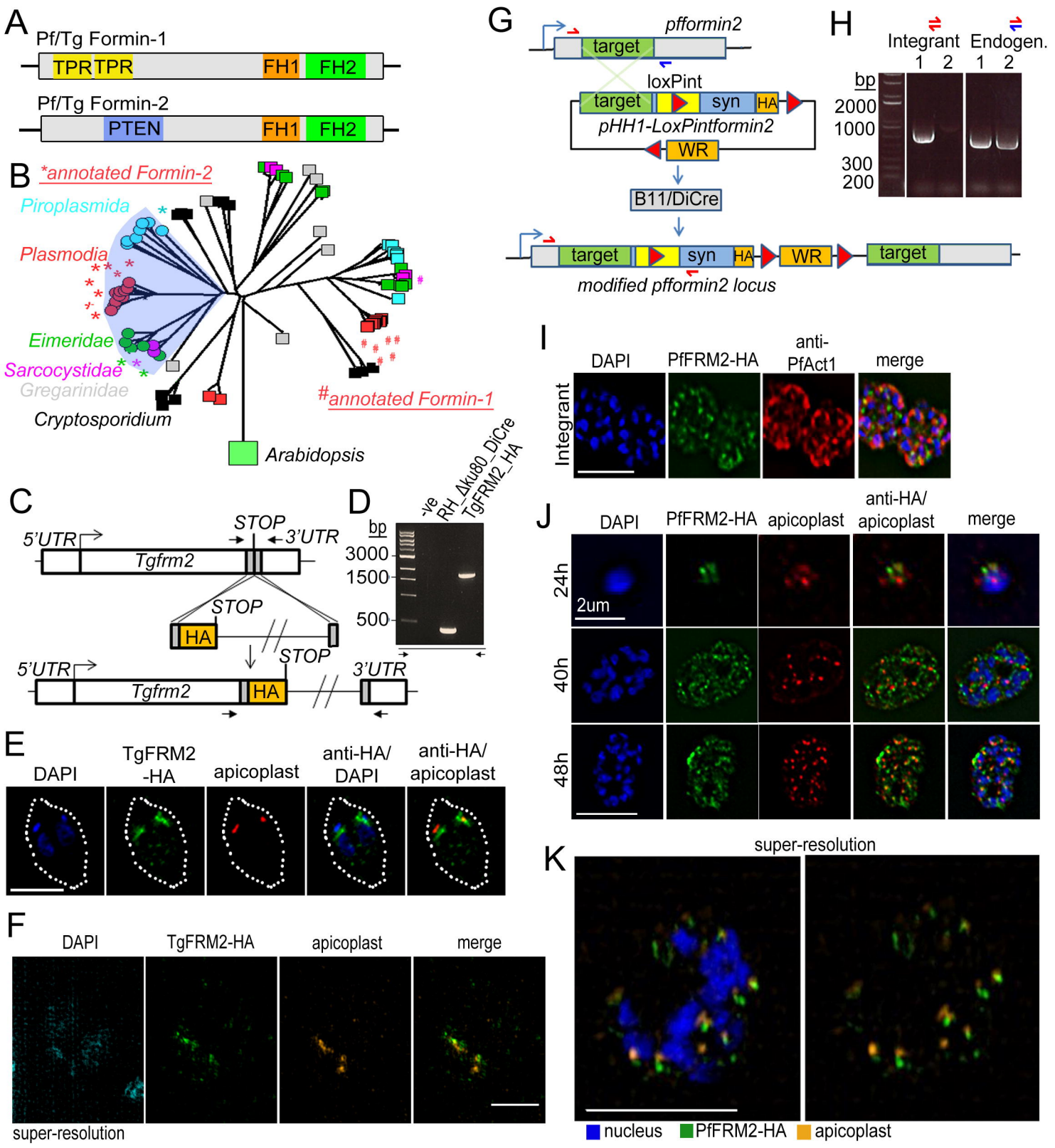
Figure 2

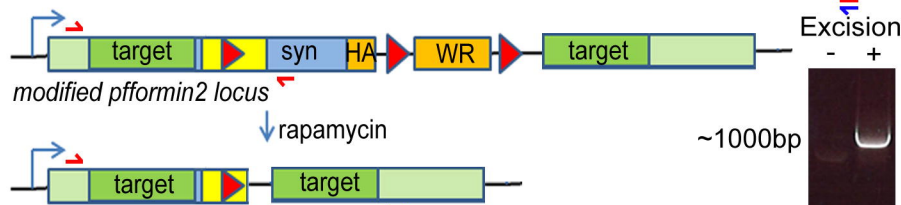
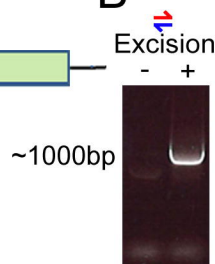
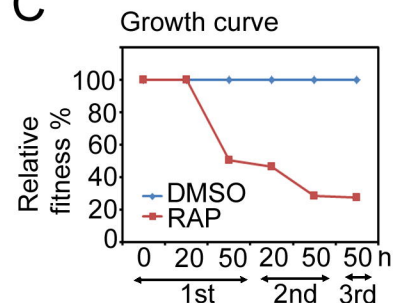
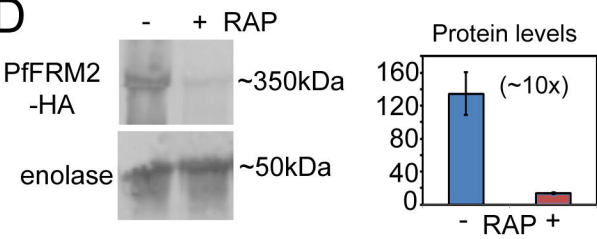
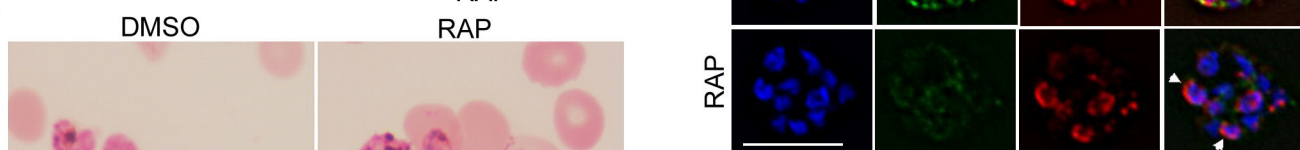
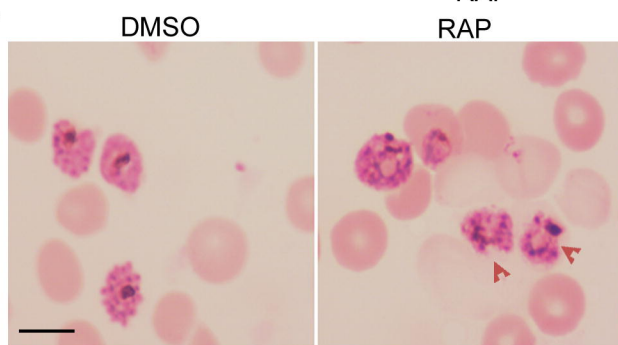
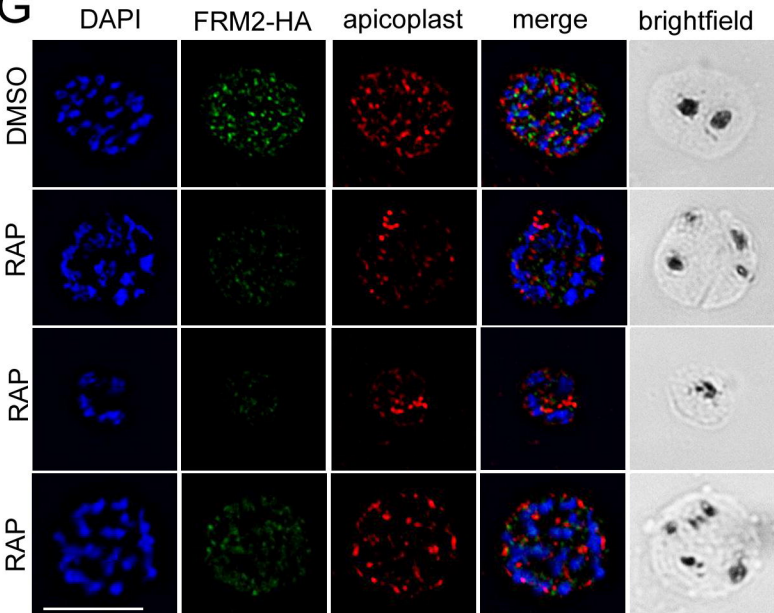
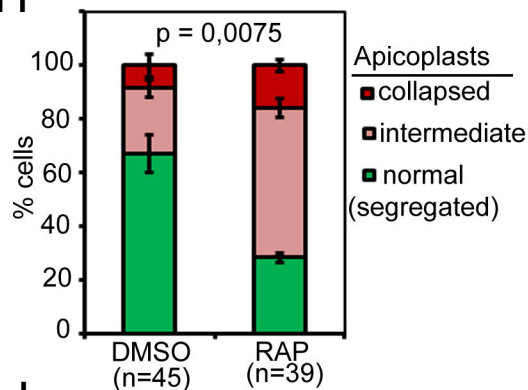
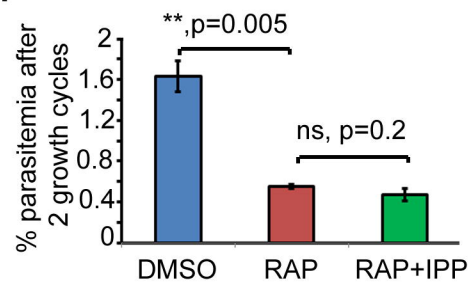


**Figure 3****A****B****C****D****E****F**



# Figure 4



**Figure 5****A****B****C****D****E****F****G****H****I**

# Figure 6

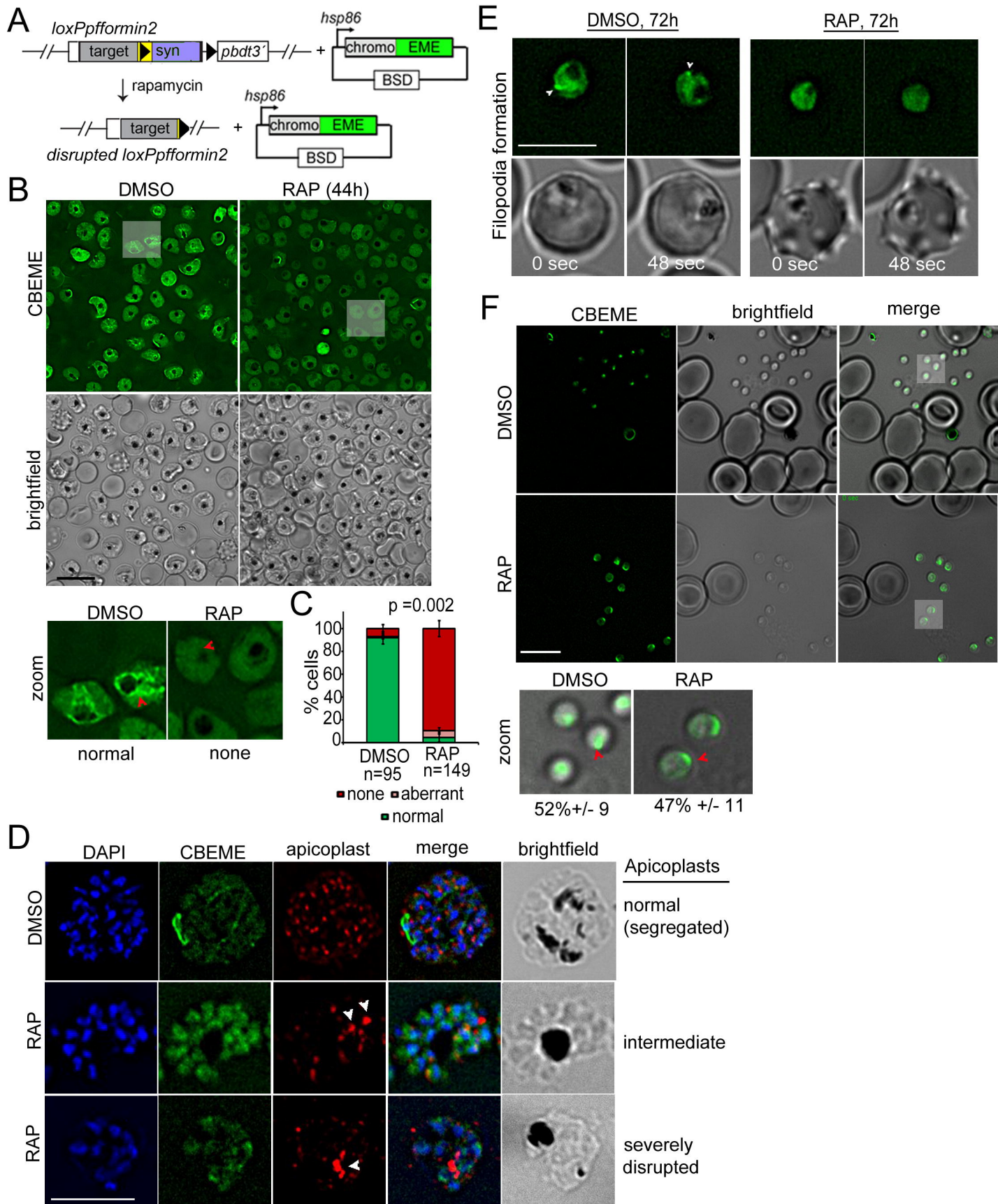
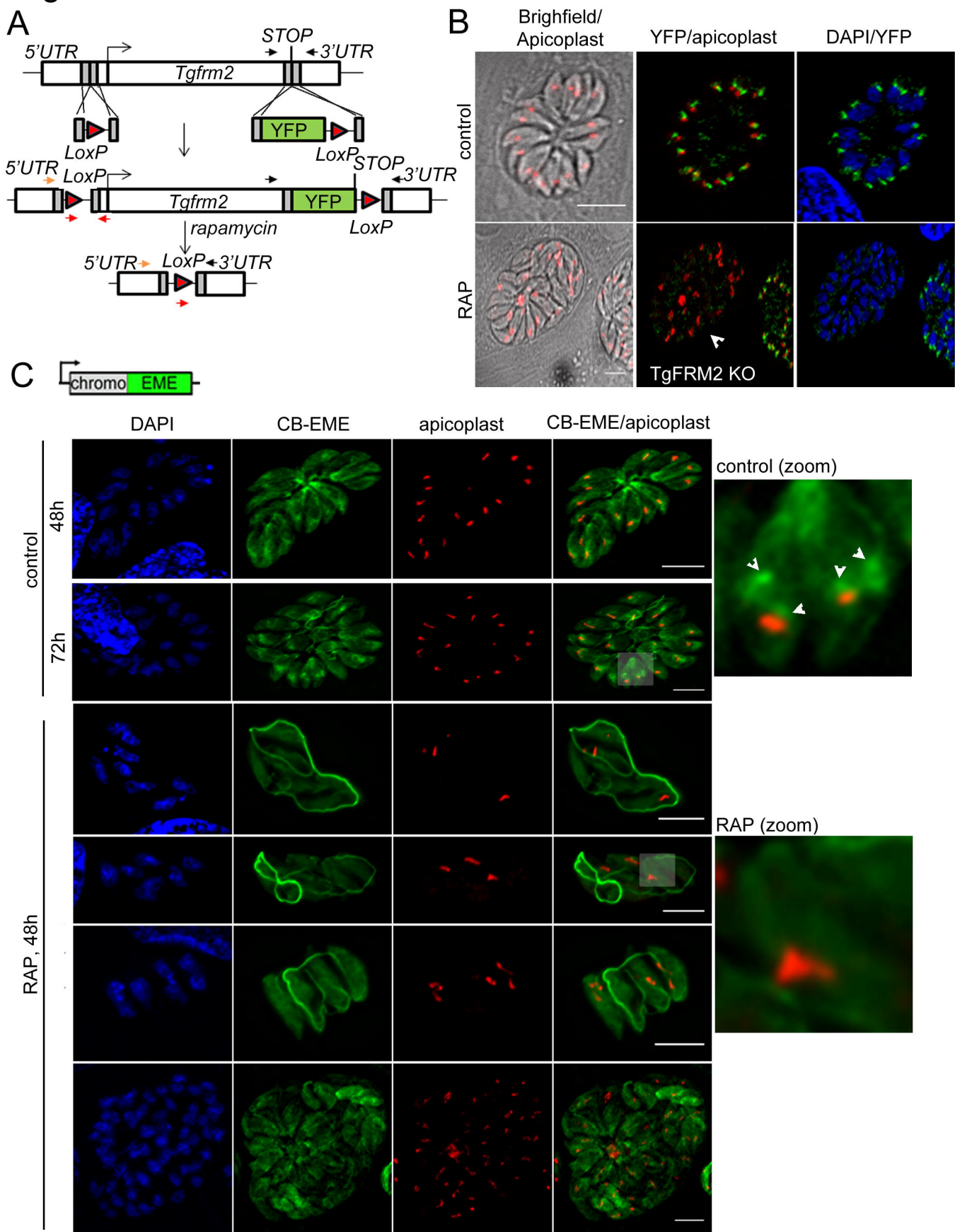


Figure 7



# Figure 8

Formin-2 WT

Formin-2 cKO

*T. gondii*

intercellular  
F-actin network

intercellular  
F-actin network  
unaffected

intracellular F-actin

apicoplasts  
disrupted

intracellular F-actin  
abrogated

*P. falciparum*

intracellular F-actin

apicoplasts  
disrupted

intracellular F-actin  
abrogated

● nucleus ● apicoplast ● Formin-2 } F-actin

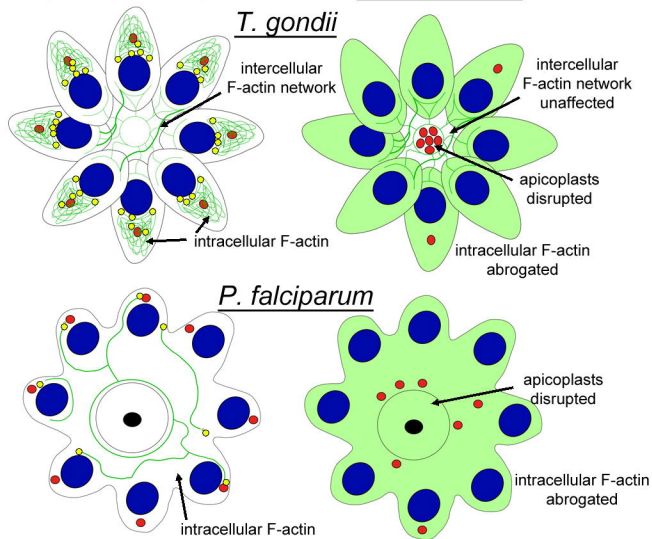
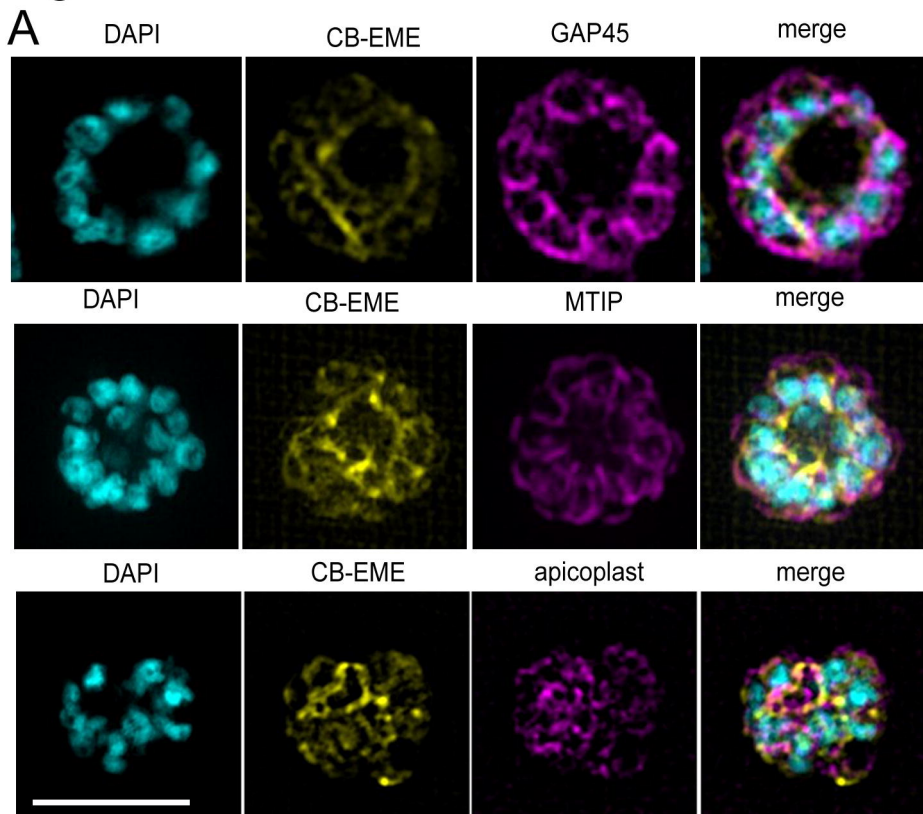


# Figure S1



**B**

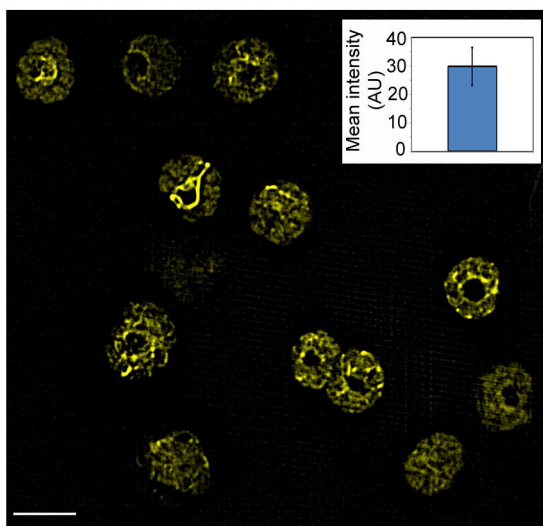


# Figure S2

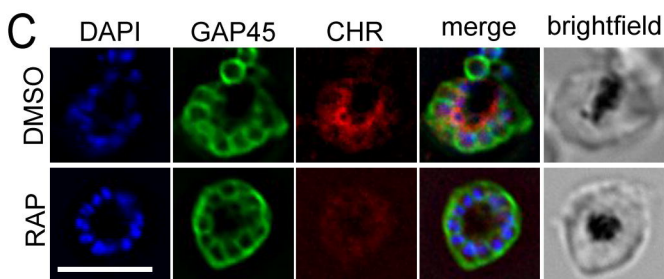
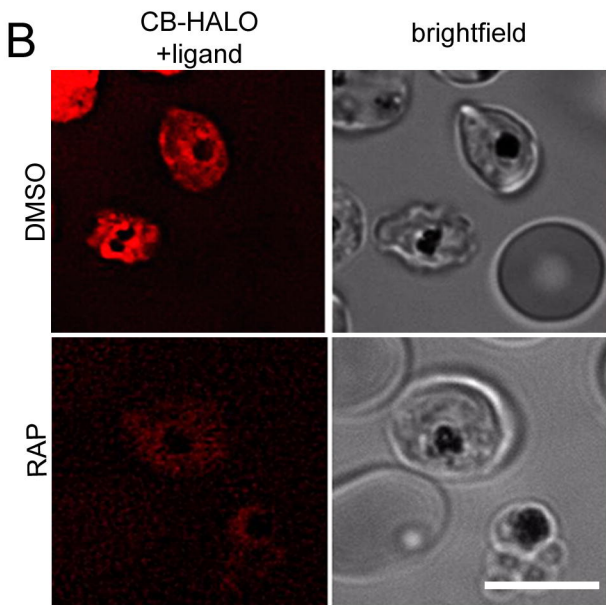
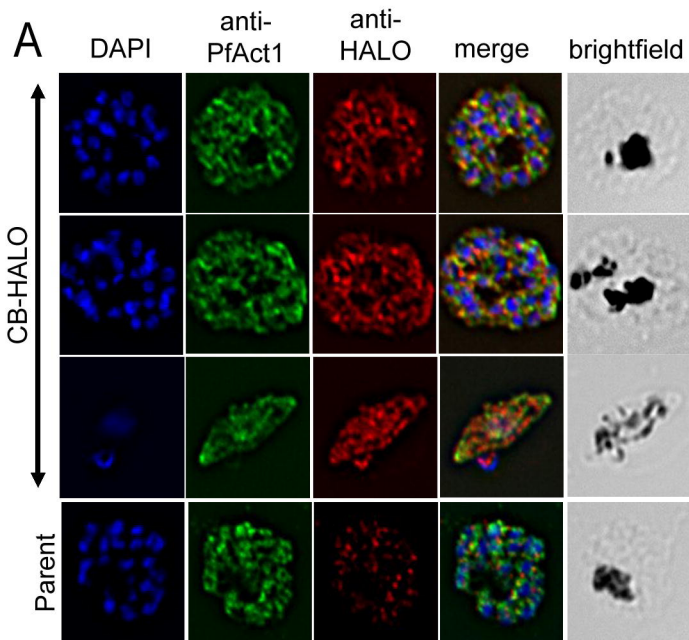
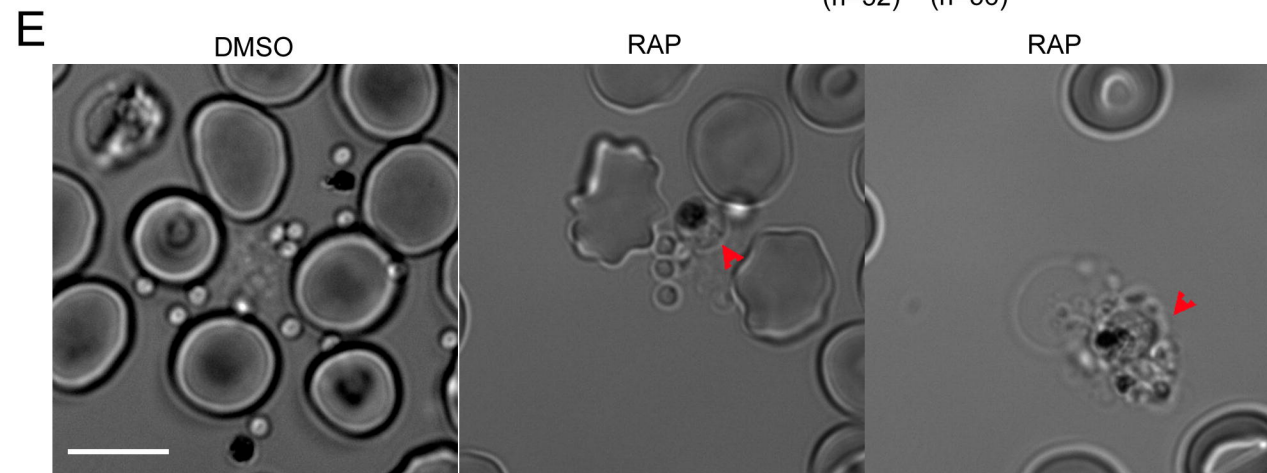
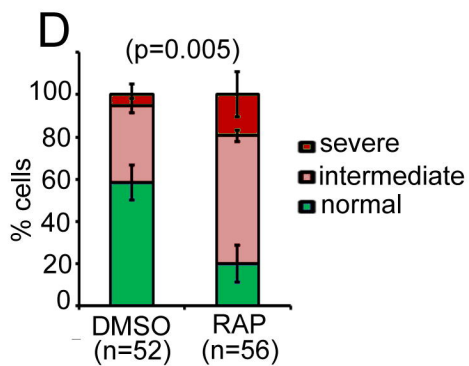
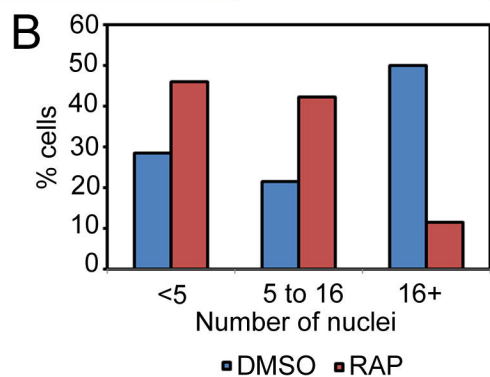
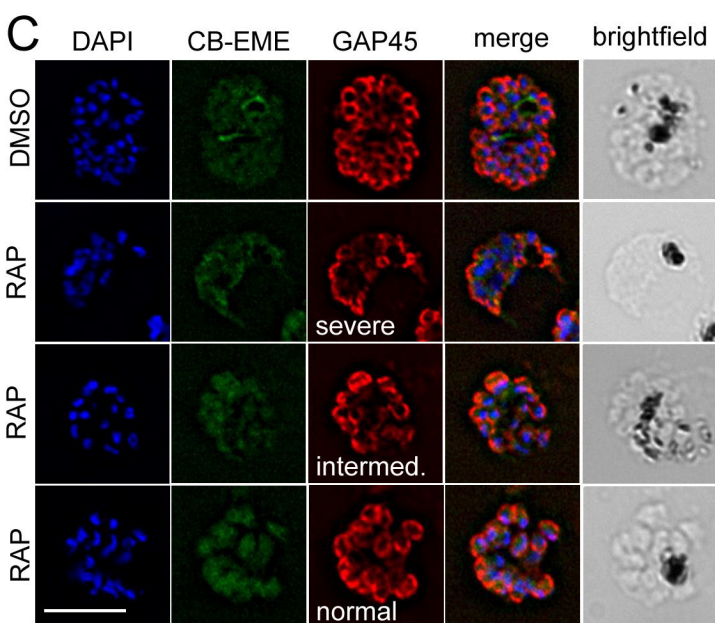
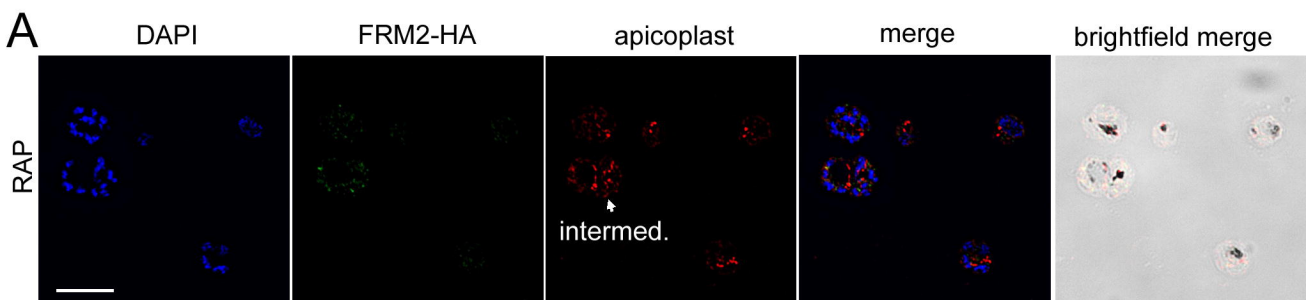
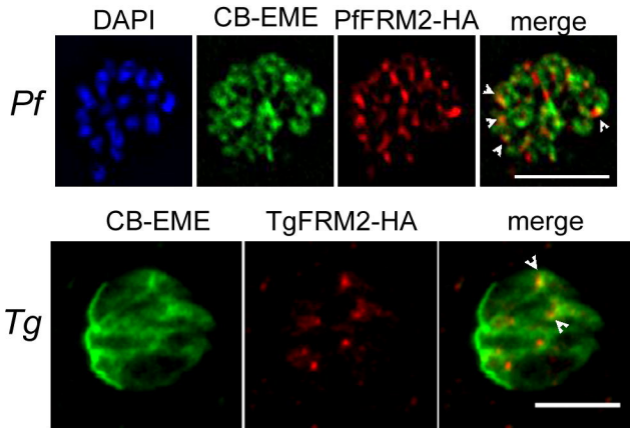


Figure S3





# Figure S4



# Figure S5

